CHALMERS
UNIVERSITY OF TECHNOLOGY

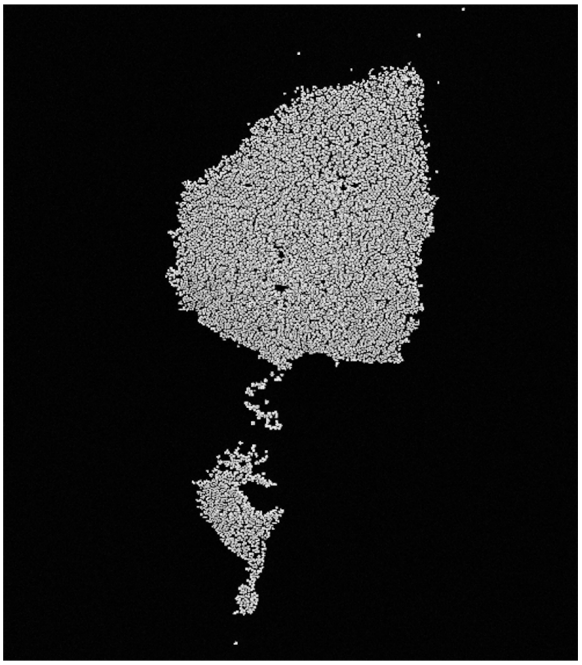

Enhancing Gas Adsorption in Gas Sensors

Gold–Platinum Bimetallic Nanoparticles and Methylated Coordination Cages

Master's thesis in Nanotechnology

MARZYEH ADVAND

DEPARTMENT OF CHEMISTRY AND CHEMICAL ENGINEERING
Division of Applied Chemistry

CHALMERS UNIVERSITY OF TECHNOLOGY
Gothenburg, Sweden 2025
www.chalmers.se

Master's thesis 2025

Enhancing Gas Adsorption in Gas Sensors

Gold–Platinum Bimetallic Nanoparticles and Methylated Coordination Cages

MARZYEH ADVAND

CHALMERS
UNIVERSITY OF TECHNOLOGY

Department of Chemistry and Chemical Engineering
Division of Applied Chemistry
Martin Andersson's research group
Chalmers University of Technology
Gothenburg, Sweden 2025

Enhancing Gas Adsorption In Sensors
Au–Pt Nanoparticles and Methylated Coordination Cages
Marzyeh Advand

Supervisor 1: Mats Hulander, Applied Chemistry, Chemistry and Chemical Engineering

Supervisor 2: Angela Beth Grommet, Chemistry and Biochemistry, Chemistry and Chemical Engineering

Examiner: Martin Andersson, Applied Chemistry, Chemistry and Chemical Engineering

Master's Thesis 2025
Department of Chemistry and Chemical Engineering
Division of Applied Chemistry
Martin Andersson (MA) research group
Chalmers University of Technology
SE-412 96 Gothenburg
Telephone +46 31 772 1000

Cover: The cover image shows an SEM micrograph of Au–Pt nanoparticles, captured by my supervisor, Mats Hulander, and me. After several experimental trials using different synthesis methods, this image marked the first successful preparation of well-dispersed Au–Pt nanoparticles. The SEM image resembles a hand holding a leaf. To highlight this visual resemblance, I generated an artistic illustration using ChatGPT and placed it beside the original SEM image.

Typeset in LaTeX
Printed by Chalmers Reproservice
Gothenburg, Sweden 2025

Enhancing Gas Adsorption in Gas Sensors
Gold–Platinum Bimetallic Nanoparticles and Methylated Coordination Cages
MARZYEH ADVAND
Department of Chemistry and Chemical Engineering, Division of Applied Chemistry
Chalmers University of Technology

Abstract

This thesis investigates two nanostructured materials, bimetallic gold platinum (AuPt) nanoparticles and a methylated cobalt(II)/iron(II) coordination cage, for their potential use in gas sensors designed to detect acetone, a key biomarker for non-invasive glucose monitoring.

The AuPt nanoparticles were synthesized using a modified co-reduction method based on Britto's procedure. The synthesis was optimized to achieve uniform and well-dispersed nanoparticles through precise control of reaction time and washing steps. The nanoparticles were characterized using SEM and, EDX, to confirm their morphology, composition, and crystal structure. They were immobilized on quartz substrates through silane functionalization, and UV–Vis spectroscopy was used to verify both immobilization and acetone vapor adsorption. A clear spectral shift observed after acetone exposure confirmed successful adsorption on the nanoparticle surface, indicating their suitability for gas sensing applications.

In parallel, methylated Co(II) and Fe(II) coordination cages were synthesized through subcomponent self-assembly and characterized using NMR and UV–Vis spectroscopy. The immobilization of Co(II) cages on glass and silicon substrates was verified using UV–Vis and TOF-SIMS. The data is consistent with successful immobilization of the cages on both glass and silicon surfaces. Notably, this study demonstrates for the first time that this particular cage has been successfully adsorbed onto glass and silicon substrates. Gas exposure experiments were performed on the Fe(II) cage solutions and analyzed by NMR; however, no significant spectral changes were detected, likely due to gas dissipation or weak interactions at ambient conditions.

Overall, the study presents promising results for the AuPt nanoparticles, while preliminary findings for the coordination cages indicate the need for further optimization. These results contribute to the development of nanostructured materials for more sensitive and selective gas-sensing technologies aimed at advancing non-invasive diagnostic methods.

Keywords: AuPt nanoparticles, Bimetallic nanomaterials, Coordination cages, Gas sensing, Acetone detection, UV–Vis spectroscopy, Surface immobilization, TOF-SIMS, NMR spectroscopy, Non-invasive diagnostics.

Acknowledgements

A heartfelt thank you to Professor Martin Andersson for giving me the opportunity to work on a topic I am deeply passionate about and for his unwavering support throughout this journey. Your trust in my curiosity and your understanding in allowing me to pursue a research topic that is deeply connected to my heart have meant more than words can express. Your professionalism and kindness have left an everlasting impression on my life. You are truly one of a kind, Martin!

My warmest thanks to Dr. Mats Hulander for his invaluable guidance in the lab, thoughtful discussions, and continuous teaching and support. Working with you has been both inspiring and highly informative.

I would also like to thank Dr. Angela Beth Grommet for her guidance and supervision, and Ebba Matic for sharing her expertise in the organic chemistry lab and providing her methodology for investigation into potential future applications in gas sensing. Special thanks to Per Malmberg for performing the TOF-SIMS characterization, Michal Strach for conducting the XRD analysis, and Mathilde Luneau for her kind help with gas sample collection.

My appreciation extends to The Royal Swedish Academy of Engineering Sciences (IVA) for recognizing this research on IVA's 100 List 2024, and to Chalmers Innovation Office for their support through the verification grant that made this project possible.

I am also grateful to the Global Mentorship Program at Chalmers and Kristina Henricson Briggs for giving me the opportunity to conduct a meaningful field study in Kenya, and to the Nils Filblad Scholarship, which made it possible for me to travel to Japan and explore opportunities for advancing this research.

To the MA Research Group and the Applied Chemistry Department, thank you for your kindness, collaboration, and for creating such a positive and supportive working environment.

Finally, my deepest gratitude goes to my family, especially my husband and my beloved mother, for their endless love, patience, and encouragement to follow my dreams and never give up. You have always helped me imagine and believe in my dreams to come true. And to all my friends, thank you for your warm support and the wonderful moments we have shared along the way.

Marzyeh Advand, Gothenburg, March 2025

List of Acronyms

Below is the list of acronyms that have been used throughout this thesis listed in alphabetical order:

AuNPs	Gold nanoparticles
AuPt	Gold–Platinum (Bimetallic)
UV-VIS	Ultraviolet – Visible spectroscopy
SEM	Scanning Electron Microscope
TOF-SIMS	Time-of-Flight Secondary Ion Mass Spectroscopy
VOC	Volatile Organic Compound
EDX	Energy-Dispersive X-ray Spectroscopy
MQ	Milli-Q (Deionized Water)
D2O	Deuturated water
NMR	Nuclear magnetic resonance

List of Figures

1

Introduction

1.1 Background and Motivation

Non-invasive diagnostic methods are revolutionizing modern healthcare by providing patient-friendly alternatives to traditional procedures. Among these, exhaled breath analysis has emerged as a particularly promising approach due to its ability to detect volatile organic compounds (VOCs) that serve as biomarkers for various physiological and pathological conditions [1]. Acetone, for instance, is a critical biomarker for monitoring blood glucose levels, making it invaluable for diabetes management. Elevated acetone concentrations in breath correlate with ketosis, offering a non-invasive means to track metabolic states without the need for frequent blood sampling [2].

Despite its potential, the development of effective breath sensors faces significant challenges. Exhaled breath comprises a complex mixture of numerous VOCs present at trace concentrations, necessitating sensor materials with high selectivity and sensitivity to accurately detect target molecules like acetone [2, 3]. Additionally, sensors must perform reliably under varying environmental conditions, such as fluctuations in humidity and the presence of interfering substances. Current technologies, primarily based on metal oxide semiconductors, often require elevated operating temperatures and exhibit limited selectivity, which hampers their practicality for portable or wearable applications [4].

Advancements in nanomaterials offer innovative solutions to these challenges by enhancing sensor performance through improved catalytic activity, selectivity, and stability. This thesis explores two distinct classes of advanced materials, bimetallic gold-platinum (Au-Pt) nanoparticles and cobalt(II) coordination cages, each presenting unique advantages for gas sensing applications [5].

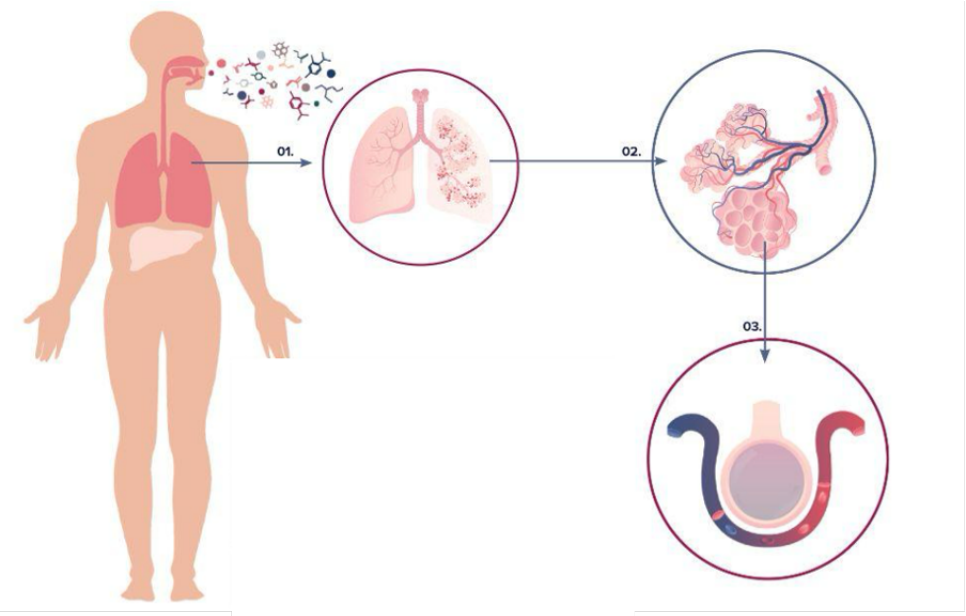

Figure 1.1: Illustration of exhaled volatile organic compounds (VOCs) and the gas exchange process in the lung alveoli.

1.1.1 Bimetallic Au-Pt Nanoparticles

Bimetallic Au-Pt nanoparticles are renowned for their synergistic catalytic properties, enhanced stability, and tunable electronic characteristics [6, 7]. Gold provides exceptional chemical inertness and strong plasmonic responses, while platinum contributes outstanding catalytic activity. When combined at the nanoscale, Au-Pt nanoparticles exhibit unique electronic and structural features that can significantly improve gas adsorption and reaction kinetics [8]. These properties are particularly beneficial for the sensitive detection of acetone and for improving selectivity toward specific VOCs. The ability to tailor the composition and morphology of Au-Pt nanoparticles allows for optimization of their sensing performance, making them ideal candidates for high-performance gas sensors [9].

1.1.2 Cobalt(II) Coordination Cages

Cobalt(II) coordination cages offer a versatile platform for selective gas adsorption through their well-defined cavities [10]. These cages can be engineered to selectively bind specific molecules based on size, shape, and chemical interactions, enhancing the selectivity of gas sensors [11]. Methylation of the coordination cages further modifies their hydrophobicity and electronic properties, increasing their affinity for target VOCs like acetone [12]. This selective binding capability ensures that sensors can distinguish acetone from other compounds in exhaled breath, thereby improving both sensitivity and specificity [13, 14]. The robustness and tunability of cobalt(II) coordination cages make them highly suitable for integration into reliable and efficient gas sensing devices [15].

1.2 Rationale for Dual Focus

Focusing on these two separate material systems allows for a comprehensive exploration of their individual contributions to gas sensor technology. Bimetallic Au-Pt nanoparticles address the need for enhanced catalytic activity and sensitivity, while cobalt(II) coordination cages tackle the challenge of selective gas adsorption [7, 16]. By investigating each material independently, this thesis aims to optimize their synthesis, characterization, and immobilization processes to maximize their respective sensing capabilities. This dual approach not only advances the understanding of each material's potential in gas sensing applications but also lays the groundwork for future integrations that could combine their strengths for even greater performance enhancements.

1.3 Purpose and Aim

The aim of this master's thesis is to synthesize and characterize two distinct nanomaterials, bimetallic gold-platinum (Au-Pt) nanoparticles and cobalt(II) methylated coordination cages, with significant potential for adsorbing target gas molecules such as acetone. This research investigates the capability of these materials to enhance gas sensor devices by improving their selectivity and sensitivity, which are crucial for accurate detection of biomarkers in exhaled breath.
To achieve this, the thesis focuses on the following objectives:

- **Synthesis and Characterization**
  - **Bimetallic Au-Pt Nanoparticles:** Develop reproducible methods for synthesizing Au-Pt nanoparticles and characterize their structural [7].And gas adsorption properties using Scanning Electron Microscopy (SEM), Energy-Dispersive X-ray Spectroscopy (EDX), X-ray Diffraction (XRD), and Quartz Crystal Microbalance (QCM).
  - **Cobalt(II) Coordination Cages:** Synthesize Fe(II) and Co(II) coordination cages following established protocols [17]. Characterize these cages using Nuclear Magnetic Resonance (NMR) and Ultraviolet-Visible (UV-Vis) spectroscopy, and confirm their successful immobilization on glass and silicon substrates through UV-Vis spectroscopy and Time-of-Flight Secondary Ion Mass Spectrometry (TOF-SIMS).

- **Immobilization and Integration**
  Investigate effective methods for immobilizing the synthesized nanomaterials onto sensor substrates, such as silicon, ensuring stable and uniform coatings that are essential for reliable sensor performance.

- **Gas Interaction Studies**
  Develop experimental setups to introduce targeted gas molecules into solu-

tions containing the coordination cages and perform NMR experiments to study host–guest interactions [18]. Evaluate the adsorption capacity and selectivity of the Au-Pt nanoparticles and coordination cages for acetone and other relevant volatile organic compounds (VOCs).

- **Evaluation of Sensor Performance**
  Assess the potential of the synthesized nanomaterials to enhance gas sensor applications by measuring their sensitivity and selectivity in detecting acetone. Utilize characterization tools and gas adsorption studies to determine the effectiveness of these materials in improving sensor performance.

Through these objectives, this thesis aims to investigate whether the synthesized AuPt nanoparticles and cobalt(II) coordination cages are potential candidates for enhancing gas sensor technologies. The successful development and integration of these nanomaterials are expected to contribute to the advancement of non-invasive diagnostic tools, particularly for monitoring critical health biomarkers through exhalation breath, like acetone, thereby supporting better health management and disease monitoring.

2

Theory

This chapter gives the scientific background used later in the thesis. First, it explains how bimetallic Au–Pt nanoparticles form by co-reduction, why they show a visible plasmon band (LSPR), and how surface interactions can shift this signal. Next, it introduces supramolecular coordination cages, metal ions, and ligands that self-assemble to form host structures that can bind small molecules, such as acetone. The chapter also outlines the surface chemistry used to attach both materials to glass or silicon and why immobilization matters for sensing. Finally, the principles behind the main techniques used in this thesis, UV-vis, NMR, SEM/EDX, XRD, and TOF-SIMS are summarized so that the results can be clearly interpreted.

2.1 Bimetallic Gold-Platinum (Au-Pt) Nanoparticles in Gas Sensing

2.1.1 Introduction to Bimetallic Nanoparticles

Bimetallic nanoparticles have gained significant attention in nanotechnology due to their synergistic properties, which often exceed those of their monometallic counterparts [7]. The combination of two metals at the nanoscale enables tunable electronic structures, enhanced catalytic activity, and improved stability, making them ideal for applications in catalysis, sensing, and energy storage [19]. Among various bimetallic systems, gold-platinum (Au-Pt) nanoparticles stand out because of their unique physicochemical properties, especially in gas sensing applications [20].

2.1.2 Structural and Electronic Synergy in Au-Pt Nanoparticles

Gold (Au) and platinum (Pt) each possess distinct characteristics that contribute to the performance of bimetallic nanoparticles:

- **Gold (Au):** Exhibits high chemical stability, excellent biocompatibility, and strong surface plasmon resonance (SPR) properties, which can enhance signal transduction in sensing applications [7].
- **Platinum (Pt):** Is renowned for its superior catalytic activity, particularly in oxidation and reduction reactions, making it highly effective for gas adsorption and reaction mechanisms [7].

When combined into a bimetallic nanostructure, Au and Pt form an alloy or core-shell configuration, modifying their electronic structure and surface energy, which

can enhance gas adsorption and improve selectivity in sensing [19].

2.1.3 Synthesis Approaches for Au-Pt Nanoparticles

The synthesis of Au-Pt nanoparticles requires precise control of size, morphology, and composition to optimize their performance in gas sensing. Several methods are commonly employed:

- **Co-Reduction Method:** Simultaneous reduction of gold and platinum precursors using a reducing agent (e.g. sodium borohydride, ascorbic acid) to obtain alloyed nanoparticles.
- **Seed-Mediated Growth:** Preformed Au nanoparticles serve as nucleation sites for Pt deposition, forming core-shell or alloyed structures.
- **Thermal Decomposition:** Uses high-temperature decomposition of metal precursors in stabilizing agents to control particle growth.

These techniques allow for fine-tuning of the Au-to-Pt ratio, which directly affects catalytic properties, gas adsorption efficiency, and sensor sensitivity [7].

2.1.4 Washing Process for Bimetallic Au–Pt Nanoparticles

To purify bimetallic Au–Pt nanoparticles after synthesis, a centrifugation-based washing procedure is employed to remove residual reagents such as ascorbic acid and sucrose. These by-products can interfere with nanoparticle characterization and performance if not adequately eliminated. Through repeated centrifugation and resuspension in Milli-Q (MQ) water, soluble impurities are separated from the denser nanoparticles, yielding cleaner suspensions. This purification step is essential to ensure consistent morphology, surface chemistry, and reproducibility in subsequent analytical and sensing applications [21].

2.1.5 Gas Sensing Mechanism of Au-Pt Nanoparticles

Bimetallic Au-Pt nanoparticles exhibit strong catalytic activity and high surface reactivity, making them excellent candidates for gas sensing applications [9]. Their mechanism involves several key processes. Target molecules, such as acetone, interact with the surface of Au-Pt nanoparticles via physisorption or chemisorption. Because of the unique electron distribution in Au-Pt systems, gas adsorption leads to changes in work function, conductivity, or surface potential, which can be detected by a sensing device. Pt facilitates oxidation/reduction reactions, while Au stabilizes the nanoparticle structure and enhances adsorption efficiency, leading to a stronger and faster sensor response [9].
The synergistic effect of Au and Pt ensures improved sensitivity, selectivity, and stability in detecting volatile organic compounds (VOCs), particularly acetone; a key biomarker for diabetes monitoring in breath analysis [22].

2.1.6 Advantages of Au-Pt Nanoparticles in Gas Sensors

The integration of Au-Pt nanoparticles in gas sensors offers multiple advantages:

- **High Selectivity:** The combination of Au and Pt allows for selective adsorption of specific VOCs, reducing interference from other gases.
- **Enhanced Sensitivity:** The catalytic activity of Pt accelerates gas interactions, leading to rapid sensor response.
- **Chemical Stability:** Gold prevents oxidation and degradation of the nanoparticle structure, ensuring long-term sensor performance.
- **Tunable Properties:** Changing the Au–Pt ratio allows the sensing behavior to be tuned for different gases and operating conditions.

By leveraging their unique catalytic and electronic properties, bimetallic Au-Pt nanoparticles continue to be a leading candidate for next-generation gas sensors, particularly in biomedical and environmental monitoring applications [9].

2.1.7 Characterization of Bimetallic Au-Pt Nanoparticles

To evaluate the morphology, composition, and structural properties of the synthesized bimetallic gold-platinum (Au-Pt) nanoparticles, three primary characterization techniques were used: Scanning Electron Microscopy (SEM), Energy-Dispersive X-ray Spectroscopy (EDX), and X-ray Diffraction (XRD) [23].

2.1.7.1 Scanning Electron Microscopy (SEM) for Morphology Analysis

Scanning Electron Microscopy (SEM) was used to analyze the size, shape, and dispersion of the synthesized Au-Pt nanoparticles. The high-resolution SEM images provided confirmation of particle morphology, ensuring that the nanoparticles were well-formed and not aggregated. Size distribution analysis was performed to confirm the uniformity of the nanoparticles and thereby assess the reproducibility of the synthesis. Furthermore, the surface characteristics were evaluated to detect any irregularities or defects that could affect gas adsorption behavior. The SEM images revealed that the synthesized Au-Pt nanoparticles were well-dispersed, uniform in size, and exhibited a consistent morphology, confirming the effectiveness of the synthesis process [24].

2.1.7.2 Energy-Dispersive X-ray Spectroscopy (EDX) for Elemental Composition

To confirm the presence and composition of gold and platinum within the nanoparticles, Energy-Dispersive X-ray Spectroscopy (EDX) was conducted in conjunction with SEM. This technique provided elemental confirmation, identifying the presence of both Au and Pt in the nanoparticles. [25]

2.2 Supramolecular Coordination Cages

2.2.1 Supramolecular Chemistry: Principles and Applications

Supramolecular chemistry, often referred to as "chemistry beyond the molecule" [26], focuses on the assembly of molecular systems through non-covalent interactions, such as hydrogen bonding, electrostatic forces, and van der Waals interactions [27]. Unlike conventional chemistry, where molecules are formed through strong covalent bonds, supramolecular chemistry relies on weaker interactions to create complex architectures with distinct properties [27]. These weak interactions often impart unique characteristics, such as self-healing ability, responsiveness to external stimuli, and dynamic adaptability, making supramolecular systems highly versatile for various applications, including sensing, catalysis, and molecular separations [28].

One of the foundational concepts of supramolecular chemistry is host-guest recognition, which is based on a "lock-and-key" mechanism, where a guest molecule selectively fits within a host structure. This principle was first introduced by Emil Fischer in 1894 to explain enzymatic activity and later expanded to artificial molecules in the 1960s [27]. Key breakthroughs in the field came from Charles Pedersen, Donald Cram, and Jean-Marie Lehn, whose pioneering work in host-guest chemistry led to the development of novel supramolecular systems and earned them the Nobel Prize in Chemistry (1987).

Over time, supramolecular chemistry has expanded significantly, leading to the discovery of various molecular architectures, including rotaxanes, catenanes, metal-organic frameworks (MOFs), micelles, vesicles, and coordination cages. Many of these systems are self-assembled, meaning that they spontaneously form stable structures when the right molecular components are combined under suitable conditions. This self-assembly process is primarily governed by thermodynamics, where the final product represents the most stable configuration, although kinetic factors can sometimes lead to metastable structures [27]. Among these supramolecular systems, coordination cages have emerged as particularly promising materials due to their well-defined cavities, tunable chemical properties, and ability to encapsulate guest molecules.

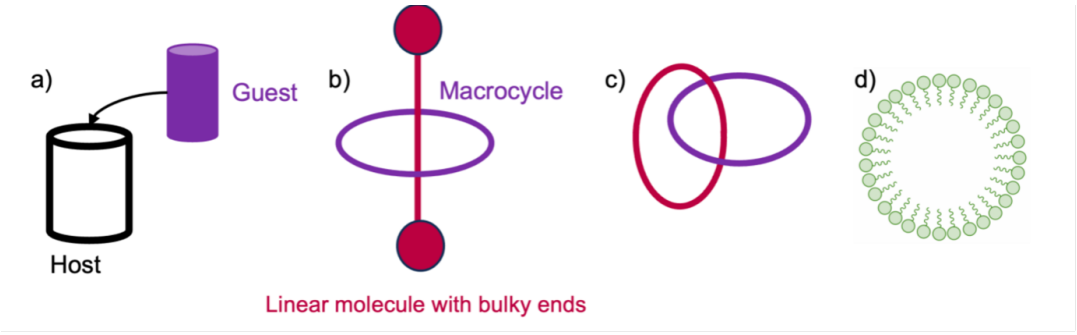

Figure 2.1: Schematic representations of some supramolecules. **(a)** Host guest system. **(b)** Rotaxane, a linear molecule threaded through a macrocycle. **(c)** Catenane, two entangled macrocycles. **(d)** Miselle, a spherical assembly of amphiphilic molecules. [17]

2.2.2 Coordination Cages: Structure and Formation

Coordination cages are discrete molecular architectures composed of metal centers (M) interconnected by organic ligands (L), forming well-defined three-dimensional frameworks [30]. The metal-ligand interactions primarily involve coordinative bonds, which are stronger than weak non-covalent interactions (such as van der Waals forces) but weaker than covalent bonds. The strength of these bonds typically falls within the range of 15–60 kcal/mol, allowing for structural flexibility and dynamic assembly, which distinguishes coordination cages from purely covalent molecular frameworks [31].

The first tetrahedral coordination cage was reported by Saalfrank et al. in 1988, marking a significant milestone in the field [29]. Since then, numerous coordination cages with diverse geometries, sizes, and metal-ligand combinations have been synthesized, often as serendipitous discoveries during synthetic efforts. These structures can adopt a variety of architectures, including tetrahedral, octahedral, and cubic frameworks, depending on the coordination preferences of the metal centers and the spatial arrangement of the ligands [35, 33, 32].

The assembly process of coordination cages is governed by the kinetics of metal-ligand interactions and the thermodynamic stability of the final structure. The efficiency of self-assembly largely depends on the lability of the metal ions involved. More labile metal centers, such as Fe(II) and Co(II), facilitate dynamic error correction, enabling the system to undergo multiple bond rearrangements until the most stable structure is formed [17]. In contrast, more inert metals (e.g., Pt(II)) exhibit slower ligand exchange kinetics, which can hinder efficient self-assembly. In some cases, multiple structures with similar energy levels may coexist, or kinetic trapping may lead to the formation of a metastable product instead of the thermodynamically most favorable structure.

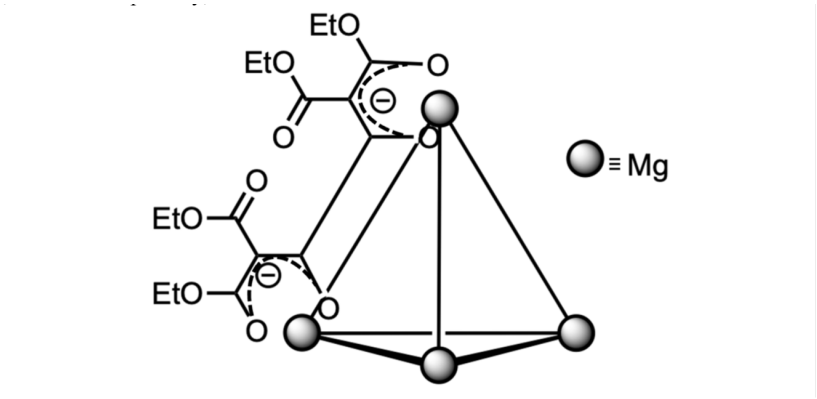

Figure 2.2: The Mg4L6 tetrahedron published by Saalfrank et al. in 1988 [29].

2.2.3 Structure and Design of Coordination Cages

Coordination cages exhibit a diverse range of geometries, structures, and sizes, which are determined by several key factors. The ability to rationally design coordination cages depends on understanding the fundamental principles that govern their formation. Two primary factors influence the final structure of a coordination cage: the geometry of the metal center and the structural properties of the ligands [30].
The metal centers in coordination cages are typically d-block metal ions, where the d-orbitals participate in bonding interactions with the ligands. The geometry of a coordination cage is largely dictated by the electronic configuration and coordination preferences of the metal ion. Depending on the number of valence electrons and how they occupy the d-orbitals, metal centers exhibit different coordination numbers and geometries, influencing how they interact with ligands.
For example:

- Iron(II) (Fe^{2+}) typically adopts an octahedral coordination geometry, where six ligands are arranged symmetrically around the metal center.
- Platinum(II) (Pt^{2+}) prefers a square planar coordination geometry, where four ligands coordinate in a two-dimensional plane.

These geometric constraints play a crucial role in determining the overall shape and stability of the final coordination cage. A metal center with predictable ligand coordination preferences enables the design of well-defined supramolecular architectures with controlled symmetry and functionality.
In addition to the metal center, the ligand structure is a major determinant of the final cage architecture [30]. Several ligand properties influence the assembly of coordination cages, including Determining how many metal centers can be incorporated. Dictates the geometric arrangement of metal-ligand interactions. Rigid, highly symmetrical ligands tend to produce more predictable structures, whereas flexible ligands can lead to diverse and sometimes unexpected assemblies. Large or bulky substituents on the ligand can restrict the types of structures that can form by preventing certain metal-ligand interactions.

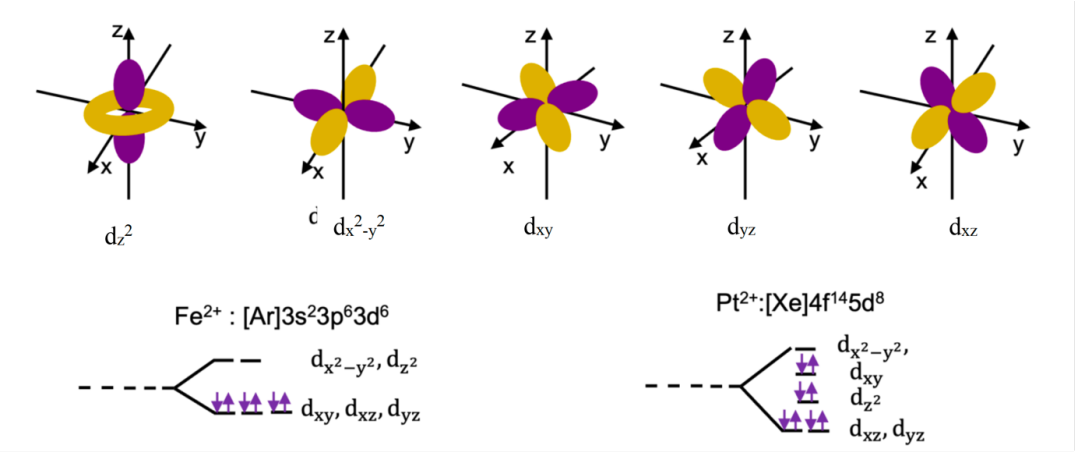

Figure 2.3: 5 different d-orbitals, and electron configurations of octahedral Fe^{2+} and square planar Pt^{2+}.

Ligands in coordination cages typically function in two primary binding modes:

- **Edge-bridging ligands**, where the ligand connects two metal centers along an edge, forming linear or polyhedral frameworks.
- **Face-capping ligands**, where the ligand binds across the face of a polyhedral structure, stabilizing the overall cage architecture [33].

Examples of coordination cages with these ligand-binding modes are illustrated in Figure 2.4, highlighting how different ligand designs lead to distinct supramolecular assemblies.

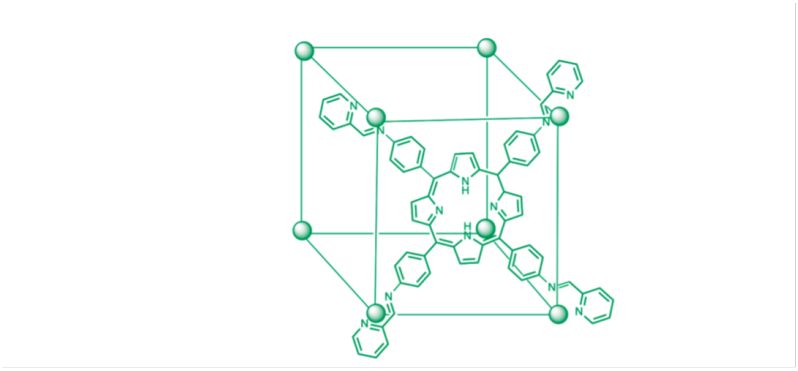

Figure 2.4: Example of a face-capped coordination cage. The ligands bridge the corners across each face [33].

2.2.4 Rational Design and Self-Assembly of Coordination Cages

Designing a coordination cage involves selecting metal-ligand combinations that predictably lead to the desired final structure. In most cases, rigid, highly symmetrical ligands are paired with metal centers of known coordination geometry to achieve a well-defined and thermodynamically stable structure.

However, since coordination cages form via self-assembly, the outcome is not always entirely predictable. The assembly process is governed by the thermodynamic stability of the system, and in some cases, multiple structures with similar energy levels may form simultaneously. Additionally, kinetic factors can influence the reaction pathway, occasionally leading to the formation of unexpected products or metastable intermediates instead of the thermodynamically most favorable structure [37].
Despite these challenges, advances in supramolecular chemistry and computational modeling are enabling more precise rational design of coordination cages, expanding their potential applications in gas sensing, catalysis, molecular encapsulation, and separations.

2.2.5 Formation of Coordination Cages Through Subcomponent Self-Assembly

Coordination cages can be synthesized through various approaches, all of which involve the combination of metal ions and organic ligands, allowing the system to self-assemble into the final structure. In this study, coordination cages are constructed via a subcomponent self-assembly reaction, a strategy that enables the formation of complex cage architectures in a single reaction step. This method involves the in situ generation of ligands through a templated Schiff base condensation reaction, where an aldehyde and an amine react in the presence of metal ions to form the desired coordination structure [38]. The reaction results in the formation of both coordinative bonds (N→M) between the ligand and metal center and dynamic covalent imine bonds (N=C) within the ligand framework, significantly increasing the complexity of the system.
A key advantage of subcomponent self-assembly is the efficiency and modularity of the process. Unlike traditional methods that require the pre-synthesis of multidentate ligands, this approach enables the formation of ligands directly within the reaction mixture, reducing synthetic effort. Additionally, the components used metal ions, aldehydes, and amines are often commercially available or easily synthesized, making this method cost-effective and scalable [38]. The modular nature of the process also allows for structural tunability, as specific properties of the final cage can be adjusted by replacing one or more subcomponents with functionalized alternatives [30].

2.2.6 Dynamic Nature and Error Correction in Self-Assembly

One of the defining features of subcomponent self-assembly is its dynamic nature, which provides a built-in error correction mechanism. The reversible nature of both the coordinative metal ligand interactions and the covalent imine bonds ensures that the assembly process continues until the most thermodynamically stable structure is achieved. If incorrect ligand-metal connections occur, the flexibility of the system allows them to dissociate and reassemble correctly over time.
The choice of metal ions plays a crucial role in this process. For effective error correction, the metal center must be kinetically labile, meaning it should allow

ligand exchange to occur at a rate that enables structural optimization. Highly labile metals, such as iron(II) (Fe^{2+}) and cobalt(II) (Co^{2+}), facilitate efficient self-correction, ensuring that the final product is well-defined and structurally robust. In contrast, more inert metal centers can lead to kinetically trapped species that may not represent the most stable conformation.

2.2.7 Acid Sensitivity and Controlled Guest Release

A notable characteristic of Schiff base-derived coordination cages is their sensitivity to acidic environments. The imine bonds (N=C) formed during ligand assembly can be hydrolyzed under acidic conditions, leading to the breakdown of the cage structure [39]. While this can be a limitation in acidic environments, it also presents a functional advantage the ability to control guest encapsulation and release. By modulating pH, the cage can be selectively assembled or disassembled, providing a responsive mechanism for applications in drug delivery, molecular transport, and controlled-release systems.

2.2.8 Functional Properties and Applications of Coordination Cages

While early research on coordination cages was driven by the synthetic challenge of constructing highly symmetrical architectures, more recent studies have focused on their functional properties, particularly their ability to bind and encapsulate guest molecules within their internal cavities. This host-guest interaction capability has led to a wide range of applications, including Coordination cages that can encapsulate reactive or unstable molecules, protecting them from degradation or unwanted side reactions. This feature has been explored in the stabilization of bioactive compounds and reactive intermediates in synthetic chemistry [31]. The confined environment within coordination cages can mimic enzyme-like catalysis by stabilizing transition states and directing reaction pathways, leading to improved selectivity and efficiency in catalytic processes [40]. Coordination cages exhibit potential for selective gas adsorption, enabling their use in gas sensing, storage, and separation technologies [41]. Their well-defined cavities and tunable metal-ligand interactions allow for the selective capture of specific molecules, including volatile organic compounds (VOCs) and medically relevant gases [42].
The size and shape-selective properties of coordination cages enable their application in separation processes, including the selective extraction of specific molecules from complex mixtures. The dynamic and reversible nature of coordination cages makes them highly versatile materials for sensor development, where guest binding events can induce detectable changes in optical, electrical, or structural properties.

2.2.9 Characterization of Coordination Cage

2.2.9.1 Nuclear Magnetic Resonance (NMR) Spectroscopy

Nuclear Magnetic Resonance (NMR) spectroscopy is a fundamental tool for characterizing coordination cages, providing insights into ligand environments, molecular

symmetry, and structural integrity. The technique is based on the interaction of nuclei with a net spin in a static magnetic field, where exposure to a radiofrequency pulse causes the nuclei to align and subsequently process at a characteristic Larmor frequency [43]. This frequency is influenced by the local magnetic environment, which depends on electron density, bonding interactions, and molecular structure.
For coordination cages containing diamagnetic metal centers, standard ^{1}H and ^{13}C NMR techniques can be used to determine the number of unique ligand environments, which helps establish the symmetry of the cage. However, cages incorporating paramagnetic metals pose a challenge due to signal broadening and chemical shift variations induced by unpaired electrons [30]. In this study, one-dimensional (1D) NMR is employed to verify ligand coordination and cage stability, while two-dimensional (2D) NMR provides additional insight into intramolecular connectivity and structural confirmation.
Additionally, NMR spectroscopy is used to confirm ligand coordination and cage formation by analyzing chemical shifts and splitting patterns in ^{1}H and ^{13}C NMR spectra and investigate host-guest interactions by detecting chemical shift variations upon exposure to gas molecules, indicating potential adsorption or encapsulation within the cage cavity.
While NMR provides valuable structural information in solution, UV-Vis spectroscopy is used in this study to confirm the successful immobilization of coordination cages on solid surfaces by comparing absorbance spectra before and after functionalization. Together, these techniques ensure that the synthesized and immobilized coordination cages retain their designed properties for gas-sensing applications.

2.2.9.2 Ultraviolet-Visible (UV-Vis) Spectroscopy for Concentration Calibration and Immobilization Confirmation

UV-Vis spectroscopy plays a crucial role in quantifying coordination cage concentration through the development of a calibration curve [44]. By measuring the absorbance of cage solutions at specific wavelengths, a calibration curve is established to correlate absorbance with concentration, enabling precise determination of the amount of cage molecules in solution. This method is particularly useful for tracking the efficiency of cage synthesis, purification, and immobilization processes.
Furthermore, UV-Vis spectroscopy is employed to confirm the successful immobilization of coordination cages on solid surfaces, such as silicon or glass substrates. A comparison of the absorbance spectra before and after surface functionalization reveals any spectral shifts or intensity changes, indicating the presence of cages on the surface. This approach provides a non-destructive and efficient method for verifying surface attachment while ensuring that the coordination cages retain their optical properties post-immobilization.

2.2.9.3 Time-of-Flight Secondary Ion Mass Spectrometry (TOF-SIMS)

Time-of-Flight Secondary Ion Mass Spectrometry (TOF-SIMS) was utilized to confirm the successful immobilization of coordination cages on the silicon substrate and to analyze their surface composition. This technique provides elemental and molec-

ular information by detecting secondary ions emitted from the sample surface upon ion beam bombardment. TOF-SIMS is particularly useful for characterizing coordination cages as it enables the quantification of immobilized species and provides spatial distribution mapping of the deposited materials [45].
TOF-SIMS confirmed the presence of the coordination cages on the silicon substrate by detecting characteristic fragment ions from the metal centers and ligand framework. The technique also quantified the number of immobilized cages, and these values were compared with UV-Vis results to evaluate the efficiency of the immobilization process. In addition, TOF-SIMS assessed the homogeneity of the surface coverage and showed whether the cages were uniformly distributed or formed localized aggregates.
By comparing the quantitative data from TOF-SIMS and UV-Vis spectroscopy, it was observed that the number of immobilized cages was in the same order of magnitude, confirming the reliability of both characterization techniques. These findings validate the efficiency and reproducibility of the immobilization strategy, ensuring that the coordination cages remain structurally intact and functionally viable for their intended applications.

3

Methods

3.1 Methods - Bimetallic Au-Pt Nanoparticles

A modified version of Britto's method was employed to synthesize bimetallic gold-platinum (Au-Pt) nanoparticles [7]. The following subsections detail the preparation of stock solutions, the step-by-step synthesis procedure, and the time-dependent sampling for morphological analysis.

3.1.1 Reagents and Stock Solutions

Reagents and stock solutions were prepared as follows. A 0.05 M gold(III) chloride stock was obtained by dissolving 0.09 g of $HAuCl_4.3H_2O$ in 5 mL of deionized water. A 0.05 M chloroplatinic acid stock was prepared by dissolving 0.12 g of $H_2PtCl_6.6H_2O$ in 5 mL of deionized water. A 0.05 M ascorbic acid solution was prepared by dissolving 0.17 g of ascorbic acid in 20 mL of deionized water. A sucrose solution was prepared by dissolving 0.12 g of sucrose in 20 mL of deionized water. Finally, a mixed ascorbic acid–sucrose (Asc–Suc) solution was prepared by combining the 20 mL ascorbic acid solution with the 20 mL sucrose solution to yield 40 mL of the mixture [7].

3.1.2 Synthesis Procedure

The synthesis proceeded as follows. First, the mixed ascorbic acid–sucrose (Asc–Suc) solution was pre-diluted by combining 1 mL of the stock with 3.33 mL of deionized water; this diluted Asc–Suc was labelled for subsequent use. Separately, 0.083 L (83 mL) of the 0.05 M gold stock solution was transferred to a suitable reaction vessel and further diluted with 10 mL of deionized water. Under continuous stirring, 0.66 L (666.6 mL) of the diluted Asc–Suc mixture was added slowly to the gold solution, after which the mixture was left undisturbed for 10 s to initiate gold-ion reduction. Next, 0.33 L (333.3 mL) of the 0.05 M platinum solution was measured and added to 10 mL of the developing gold-nanoparticle solution. A magnetic stir bar was then introduced, and the reaction was stirred gently to promote co-reduction and the formation of bimetallic Au–Pt nanoparticles.

Figure 3.1: Photograph of a vial containing freshly synthesized Au–Pt nanoparticles, exhibiting a characteristic pinkish-red coloration.

Figure 3.2 shows an SEM micrograph taken immediately after synthesis. The Au–Pt nanoparticles appear as bright, well-defined structures, whereas the surrounding low-contrast regions are most likely organic residues—unwashed sucrose or ascorbic acid—from the reaction mixture. The markedly lower signal intensity of these areas, compared with the metallic particles, supports this interpretation. To remove these organic residues, a step-wise washing protocol was carried out, as detailed in the next section.

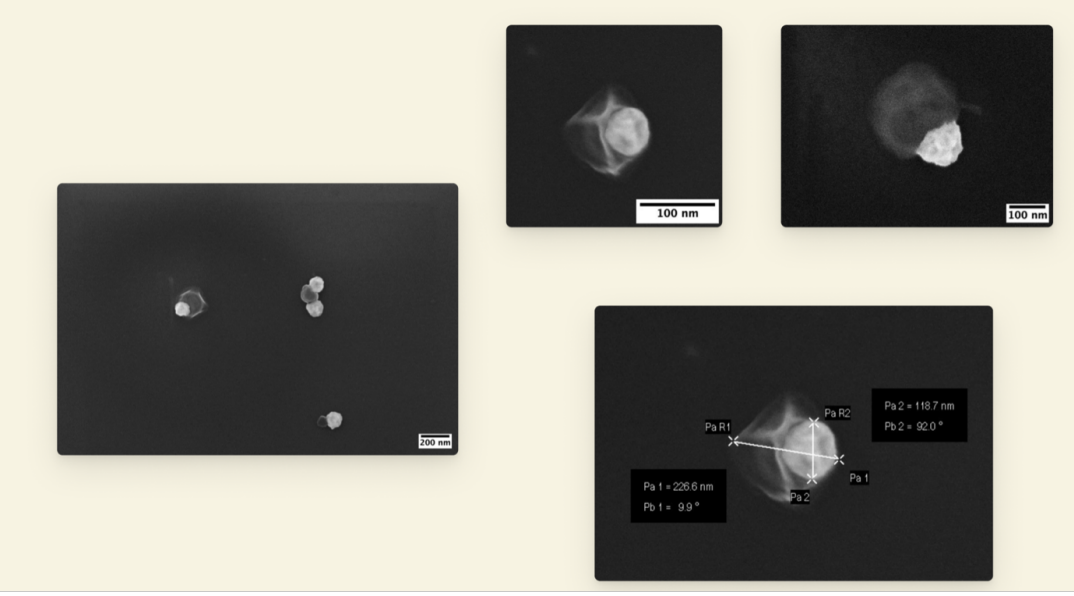

Figure 3.2: SEM images of Au–Pt nanoparticles partially attached to surrounding residues. The nanoparticles appear as bright, well-defined structures, while the less intense regions are likely organic residues such as unwashed sucrose or ascorbic acid. The lower contrast of these areas compared to the metallic particles supports this assumption.

3.1.3 Washing Process for Bimetallic Au-Pt Nanoparticles

To separate the bimetallic nanoparticles from excess ascorbic acid and sucrose, a centrifugation-based washing procedure was conducted as follows:

- Sample Distribution
  - Transfer 500 µL of the bimetallic Au-Pt nanoparticle solution and 500 µL of Milli-Q (MQ) water into a 1.5 mL Eppendorf tube.
  - Mix gently to ensure a uniform suspension.
- Centrifugation
  - Place the Eppendorf tube in a centrifuge and spin at 3×g for 5 minutes.
  - Carefully remove the supernatant, taking care not to disturb the nanoparticle pellet at the bottom of the tube.
- Repeat Washing
  - Add 1 mL of fresh MQ water to the pellet, then gently resuspend the nanoparticles by pipetting or mild vortexing.
  - Centrifuge again under the same conditions (3×g for 5 minutes), and discard the supernatant.
  - Repeat this process three times in total to thoroughly remove residual ascorbic acid and sucrose.
- Final Redispersion
  - After the final wash, transfer the remaining nanoparticle pellet into a clean 1.5 mL Eppendorf tube and resuspend in 1 mL of MQ water.
  - This final suspension contains cleaned Au-Pt nanoparticles ready for further characterization or application.

This stepwise washing process effectively removes unbound ascorbic acid and sucrose, ensuring that the bimetallic Au-Pt nanoparticles are free from excess reagents before being subjected to SEM analysis or other characterization techniques.

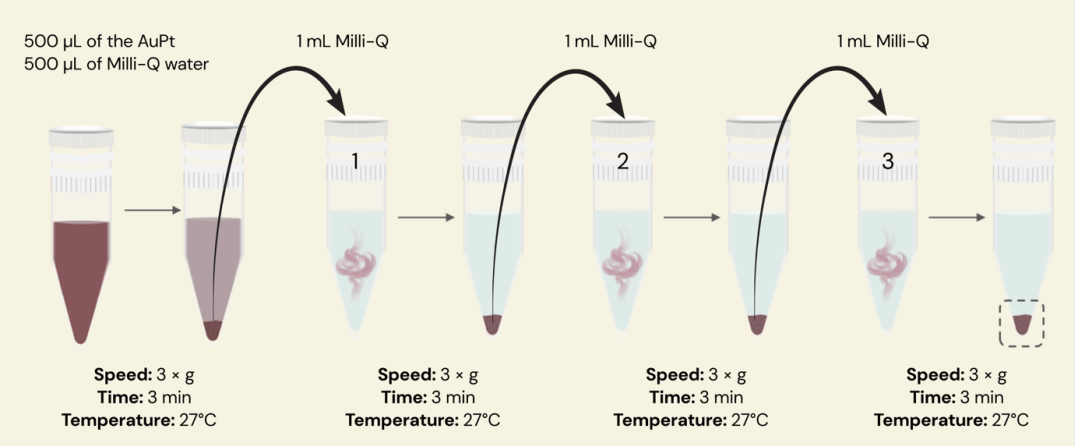

Figure 3.3: Schematic illustration of the washing process used to purify bimetallic Au–Pt nanoparticles. The nanoparticle suspension was centrifuged at 3×g for 3 minutes, repeated three times, to remove excess ascorbic acid and sucrose. After each cycle, the supernatant was discarded, and the pellet was resuspended in Milli-Q water.

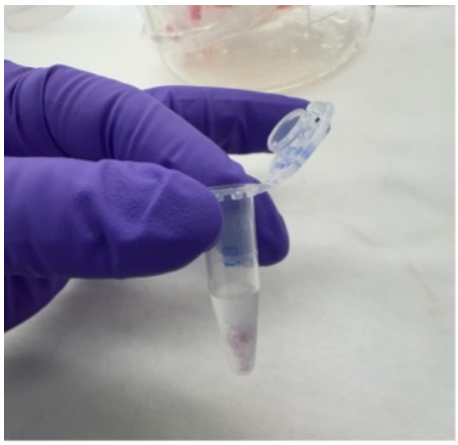

Figure 3.4: Photograph showing the final pellet of bimetallic Au–Pt nanoparticles resuspended in Milli-Q (MQ) water after the washing process. The visible pellet indicates collection and dispersion of the nanoparticles following centrifugation and removal of residual synthesis by-products.

3.1.4 Time-Dependent Observations

To study the temporal evolution of the synthesized Au-Pt nanoparticles, aliquots were collected at specific intervals and examined via Scanning Electron Microscopy (SEM):

- Right after mixing was completed.
- 1 hour after synthesis.
- 2 hours after synthesis.
- Overnight (approximately 12–24 hours) under continuous stirring.

These sampling points allowed for monitoring of particle size, morphology, and dispersion over time. By comparing SEM images at different intervals, the progression of nanoparticle formation and any potential aggregation or changes in particle size were evaluated.

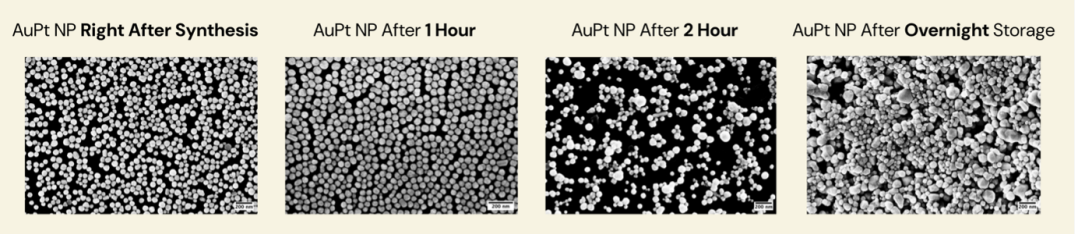

Figure 3.5: SEM images of Au–Pt nanoparticles collected at different time points following synthesis: Right after synthesis, 1 hour, 2 hours, and overnight (12–24 hours) after completion of mixing. These images illustrate the temporal evolution of particle morphology, dispersion, and size uniformity, enabling assessment of growth behavior and aggregation over time.

Analysis of SEM images collected at successive time points after synthesis revealed that the most monodisperse Au–Pt nanoparticle population—exhibiting a uniform

mean diameter—occurs approximately 1 h after completion of mixing. Particle-size distributions were quantified with FIJI (ImageJ), and the results are presented in Figure 3.6.

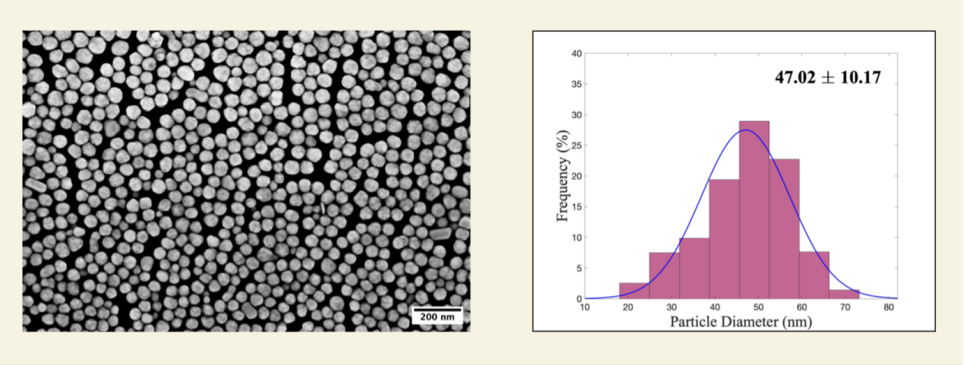

Figure 3.6: Size analysis of Au–Pt nanoparticles 1 h after synthesis. Representative SEM micrograph demonstrating a uniform, well-dispersed particle population. Corresponding particle-size histogram obtained with FIJI (ImageJ); the distribution confirms a narrow size range, indicating that the sample collected at 1 h exhibits the highest degree of monodispersity among the time points studied.

3.1.5 Immobilization of Au–Pt Nanoparticles on Quartz Glass Substrates

To investigate the gas-adsorption properties of Au–Pt nanoparticles and assess their suitability as a sensitive coating for gas-sensor structures, the particles first had to be immobilised on a solid surface. Quartz glass was chosen as the substrate because it is transparent and exhibits minimal absorbance in the same UV–Vis region as the characteristic plasmon band of the Au–Pt nanoparticles. This compatibility allows UV–Vis spectroscopy to be used to quantify both immobilisation efficiency and subsequent gas-adsorption behaviour.

UV–Vis characterisation was performed with a Thermo Scientific Multiskan GO spectrophotometer. To position the quartz slides bearing immobilised Au–Pt nanoparticles inside the cuvettes, a custom holder accommodating eight quartz layers was designed and produced by 3-D printing. The holder was printed to the exact dimensions required to secure the slides while fitting inside standard disposable plastic cuvettes, which were used for all measurements.

Eight quartz slides were first rinsed with ethanol and Milli-Q water, dried under a nitrogen stream, and then cleaned by UV/ozone exposure for 45 min. After treatment, the slides were placed in a rinsed and dried 3-D-printed holder. In parallel, a small airtight container was rinsed, dried, and equipped with a clean glass plate. Onto this plate, 500 μL of 3-mercaptopropyltrimethoxysilane and 500 μL of 94.8% methanol were quickly dispensed. The holder containing the quartz slides was immediately inserted into the container, which was then sealed and left undisturbed for 30 min to allow vapour-phase silanisation prior to Au–Pt nanoparticle immobilisation.

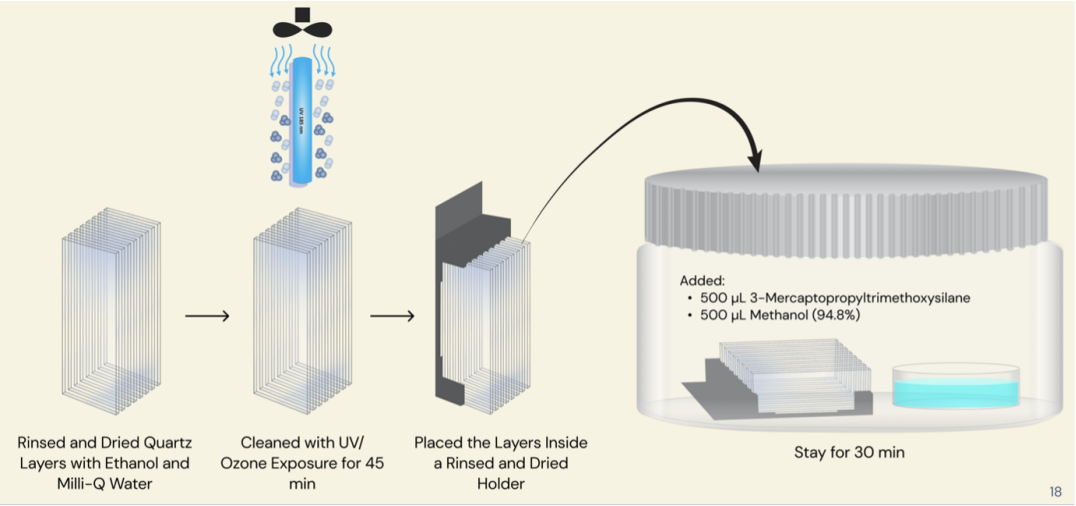

Figure 3.7: Vapour-phase silanisation workflow prior to Au–Pt nanoparticle immobilisation. Quartz slides, pre-cleaned by ethanol/Milli-Q rinse and 45 min UV/ozone treatment, are mounted in a 3-D-printed holder (left). The holder is placed inside a sealed container containing a glass plate with 500 μL 3-mercaptopropyltrimethoxysilane and 500 μL 94.8% methanol (right). The assembly is left undisturbed for 30 min, allowing silane vapour to functionalise the quartz surfaces.

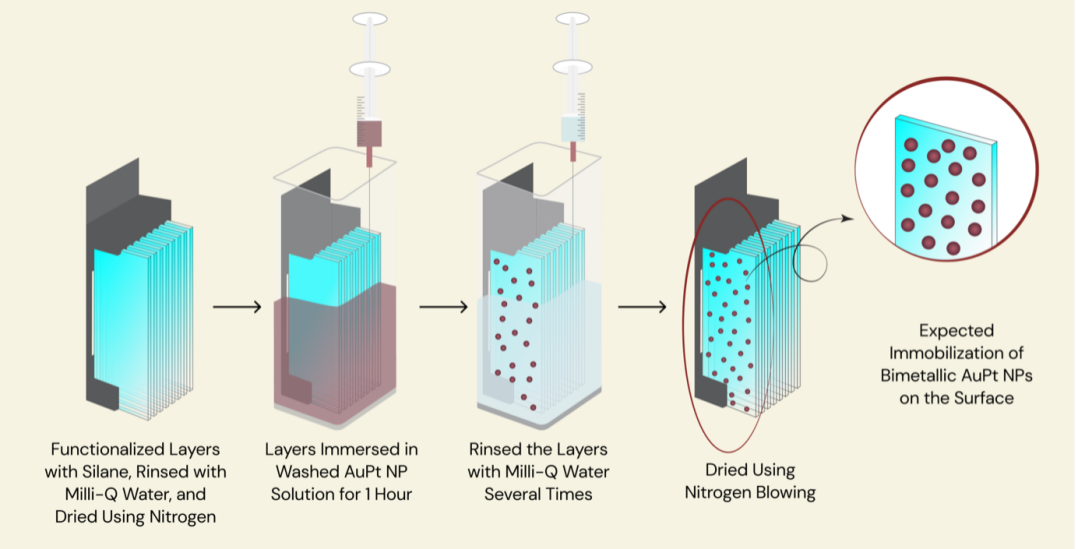

Figure 3.8: Schematic workflow for immobilizing bimetallic Au–Pt nanoparticles on quartz. Quartz slides are first silanized (3-mercaptopropyltrimethoxysilane), rinsed with Milli-Q water, and dried under N_2. The slides are then immersed in the washed Au–Pt nanoparticle suspension for 1 h, followed by multiple Milli-Q rinses and N_2 drying, yielding an Au–Pt NP layer on the surface

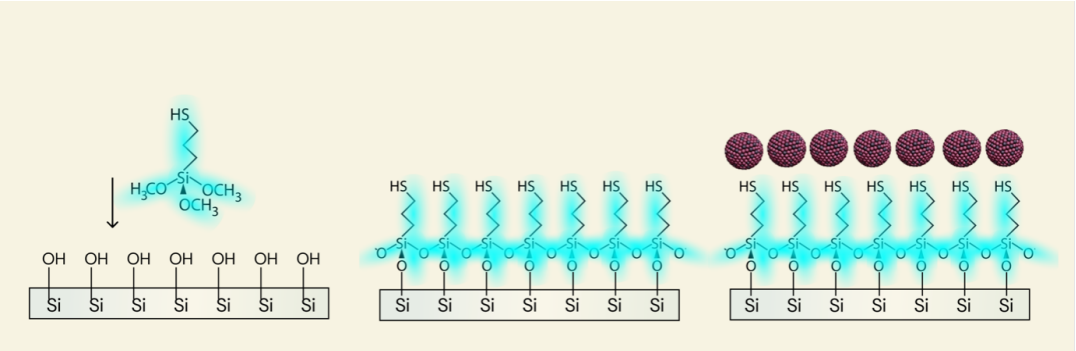

Figure 3.9: Schematic of Au–Pt nanoparticle immobilization via silanization. Hydroxylated Si/SiO_2 surface reacts with 3-mercaptopropyltrimethoxysilane (MPTMS) to form a thiol-terminated siloxane layer, after which Au–Pt nanoparticles bind to the surface through metal–thiol interactions, yielding a stable coating.

3.1.6 UV–Vis Measurements of Au–Pt Nanoparticles

Ultraviolet–visible (UV–Vis) spectroscopy records how much light a sample absorbs as a function of wavelength (typically 190–800 nm) [47]. A broadband light source passes through a monochromator (grating/prism) and adjustable slit to select a wavelength. Light is transmitted through the sample compartment (cuvette or substrate holder) to a detector; software converts transmitted intensity into absorbance. Measurements can be made in transmission for solutions and transparent films [47]. UV–Vis is fast, non-destructive, and quantitative ideal for verifying nanoparticle immobilization on transparent substrates and for tracking surface interactions (e.g., acetone uptake) through subtle LSPR changes [48]. In the Results section, the immobilisation of Au–Pt nanoparticles and their gas-adsorption behaviour are examined using UV–Vis spectroscopy and complementary techniques.

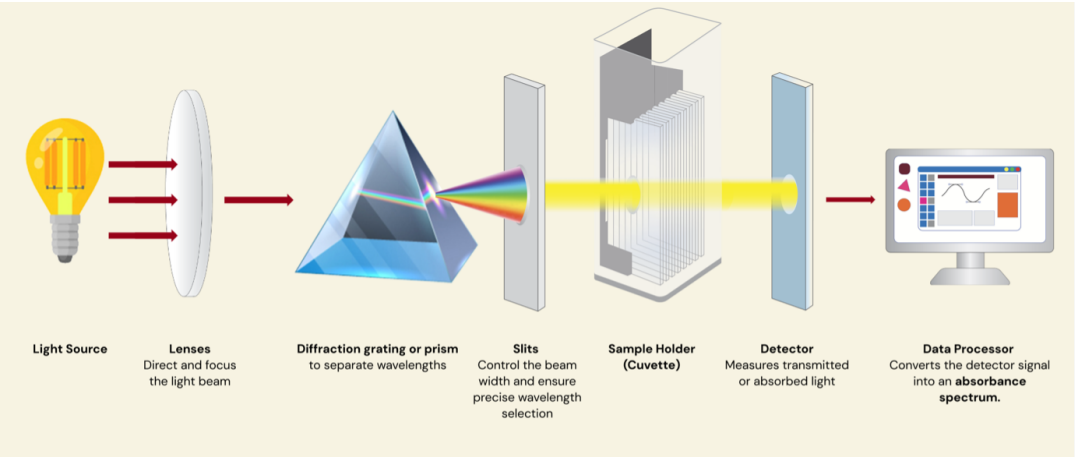

Figure 3.10: UV–Vis spectrophotometer workflow. Broadband light is collimated, dispersed by a grating/prism, narrowed by slits, passed through the sample holder (cuvette), and detected. Software converts transmitted intensity into an absorbance spectrum $A(\lambda)$. Used here to verify Au–Pt nanoparticle immobilization and to monitor acetone adsorption.

3.2 Methods – Coordination Cages

This section describes the subcomponent self-assembly of Fe(II) and Co(II) coordination cages, surface-immobilisation, and the analytical techniques used at each stage. For the synthesis of the Fe(II) and Co(II) coordination cages, all procedures followed the methodology described by E. Matic et al. in their published work. [17].

3.2.1 Formation of coordination cages through subcomponent self-assembly

There are several methods for forming coordination cages. In all of them, metal ions and ligands are combined and left to react until the cage is formed—this is the common principle behind all coordination cage assembly methods. In this work, the cages are constructed using a subcomponent self-assembly reaction. In this process, an aldehyde and an amine are combined with metal ions, and the ligand is formed in situ through a templated Schiff base condensation reaction [38].

In this reaction, both a coordinative bond (N $\rightarrow$ M) and a dynamic covalent imine bond (N=C) is formed. The in situ formation of the ligand enables a significant increase in structural complexity within a single reaction step. The subcomponents are typically commercially available or easily synthesized, which minimizes the synthetic effort compared to that required for complex multidentate ligands. Additionally, the cage structure can be easily tailored to optimize specific properties by replacing individual components [30].

Due to the dynamic nature of the bonds formed during subcomponent self-assembly, the structure can be modified after assembly through imine exchange [39]. In the assembly of coordination cages, the dynamic nature also enables a built-in error-checking process. The choice of metal ions is very important for both the assembly process and the effectiveness of the error checking. This error checking means that the assembly process continues until the thermodynamically most stable product has formed [30].

In this thesis project, two methylated coordination cages were synthesised, one employing iron(II) sulfate and the other cobalt(II) sulfate, following the procedure reported in [17]. The primary objectives were (i) to determine whether these cages can be effectively immobilised on solid substrates and (ii) to evaluate their gas-adsorption behaviour once immobilised.

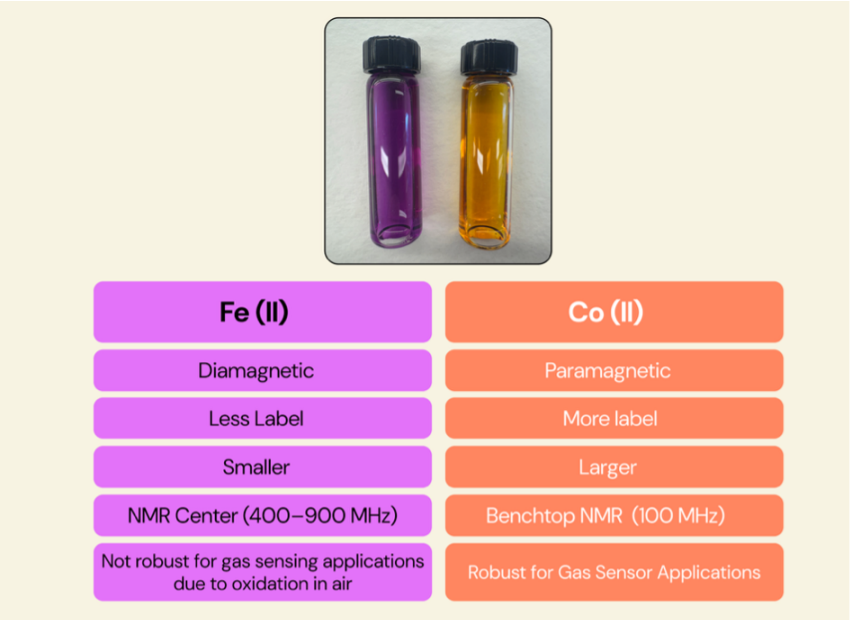

Figure 3.12: Methylated coordination cages after synthesis: Co(II) cage (orange) and Fe(II) cage (pink).

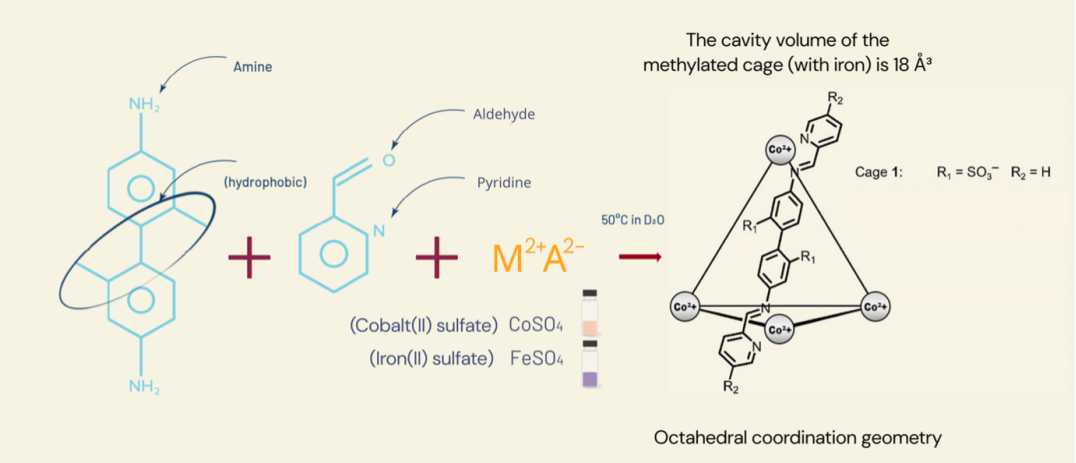

Figure 3.11: Molecular structure of the methylated Fe(II)/Co(II)$_4$ L$_6$ coordination cage

To characterise both the methylated Fe(II) and Co(II) cages, NMR spectroscopy was employed. NMR spectra reveal the number of unique ligand environments, allowing the cage symmetry to be deduced [17]. One-dimensional ^{1}H and ^{13}C NMR experiments confirmed cage formation and identified any potential breakdown products, while two-dimensional NMR techniques were used to examine atomic connectivity within the molecules.

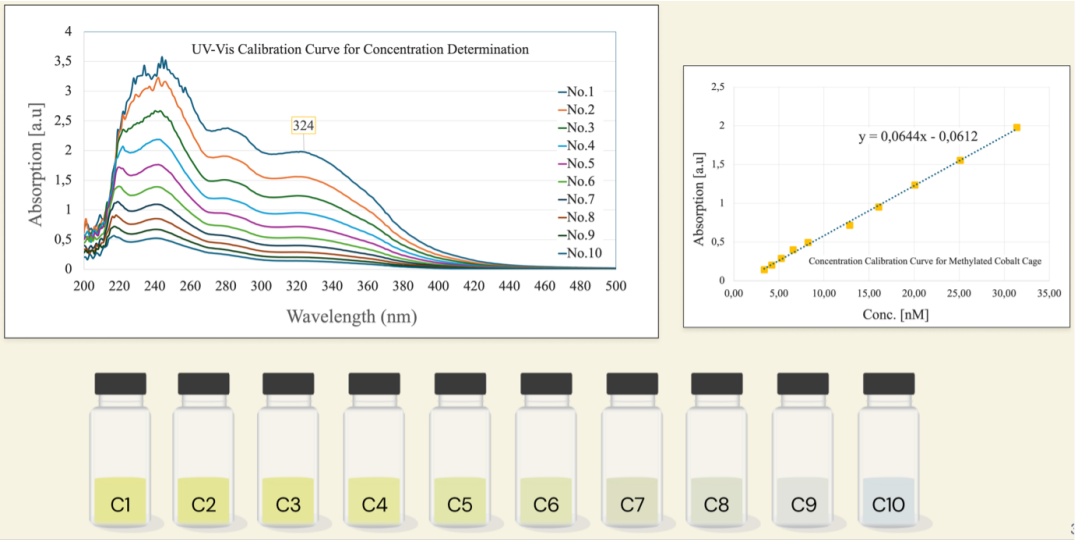

Figure 3.13: UV–Vis calibration for the methylated Co(II) cage. Left: absorbance spectra (200–500 nm) for a ten-point dilution series (C1–C10), showing a concentration-dependent band at ∼324 nm. Right: calibration plot A324 vs concentration with linear fit A=0.0644 C-0.0612 (C in nM). Bottom: vials C1–C10 used for the series. The color of the solutions in vials C1–C10 gradually changed from light yellow to essentially that of Milli-Q (MQ) water (nearly colorless).

3.2.2 Concentration Determination of Methylated Cobalt Cages

To quantify the concentration of the methylated Co(II) cage, a ten-point tenfold serial dilution (C1–C10) was prepared from a reference solution C0 = 3.14 mM. C1 was obtained by diluting 100 μL of C0 with 900 μL of Milli-Q water; each subsequent solution (C2–C10) was prepared by diluting 100 μL of the preceding solution with 900 μL of Milli-Q water. UV–Vis spectra (200–500 nm) were recorded for all dilutions, and the band at ∼324 nm was used as the analytical wavelength. Plotting A_{324} versus concentration yielded a linear Beer–Lambert relationship, A=0.0644 C-0.0612A (C in nM), which was used to determine cage concentrations and to estimate surface loadings after immobilisation.

3.2.3 Immobilization of a Co(II) Coordination Cage on a Glass Substrate

Eight glass substrates, rinsed with basic piranha solution and Milli-Q (MQ) water, were placed in a rinsed holder and dried under a nitrogen stream. The mounted slides were then immersed in a solution of the methylated Co(II) coordination cage, ensuring complete coverage of each substrate. After 48 h of incubation at room temperature, the glass slides were rinsed with Milli-Q (MQ) water and transferred to a fresh cuvette filled with MQ water. Under these conditions, immobilization of the cages on the glass surfaces was expected.

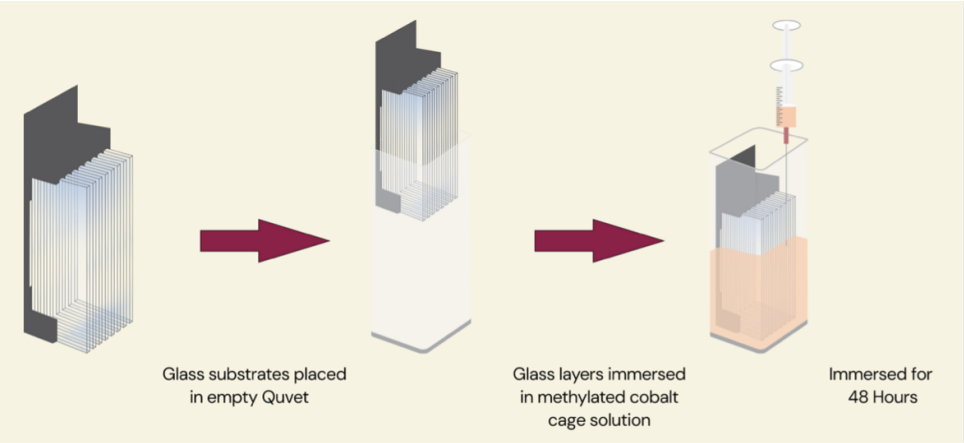

Figure 3.14: Schematic illustration of the immobilization process: Eight layers of rinsed glass substrates with basic Piranha solution and Milli-Q water are placed inside a rinsed holder. Glass substrates are placed in an empty cuvette, immersed in methylated cobalt cage solution, and incubated for 48 hours.

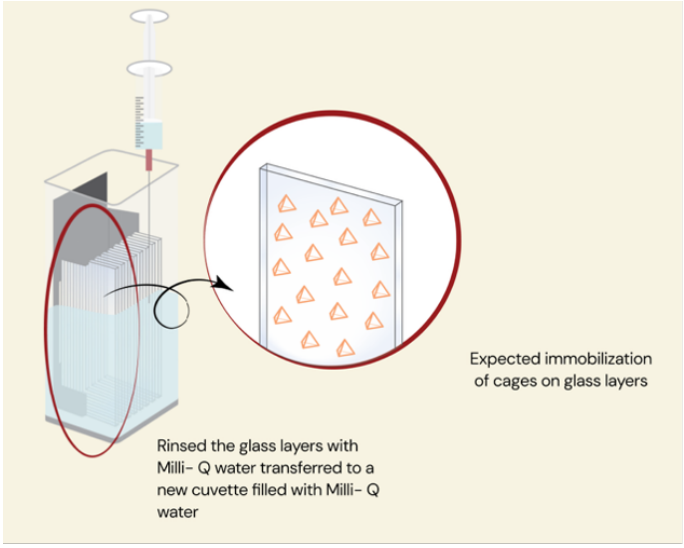

Figure 3.15: Glass layers rinsed several times with Milli-Q (MQ) water and transferred to a fresh cuvette filled with MQ water. Inset: expected immobilization of cages on the glass surfaces.

In the Results section, immobilization of the cages on glass layers was investigated using UV–Vis spectroscopy and time-of-flight secondary ion mass spectrometry (TOF-SIMS).

4

Results

This chapter presents and discusses the findings for both material systems. For the Au–Pt nanoparticles, EDX confirmed the presence of Au and Pt in the samples. UV–Vis spectroscopy was used to verify immobilization on quartz and to monitor acetone adsorption on the coatings. For the methylated Fe(II)/Co(II) cages, UV–Vis and TOF-SIMS verified immobilization on glass and silicon substrates, and NMR was used to probe gas (host–guest) interactions in solution.

4.1 Au–Pt Nanoparticles

4.1.1 Energy-Dispersive X-ray Spectroscopy (EDX)

Atomic ratio analysis was carried out to verify that the synthesized particles contained the expected Au-to-Pt ratio. The homogeneity of the particles was also assessed to ensure that gold and platinum were uniformly distributed throughout the nanoparticles. The EDX spectra confirmed the successful incorporation of both elements, and the measured atomic ratios were consistent with the intended synthesis composition [25]. EDX confirmed the presence of Au and Pt in the nanoparticles. The spectrum shows Pt M (∼2.05 keV) and Au M (∼2.12–2.20 keV) peaks.

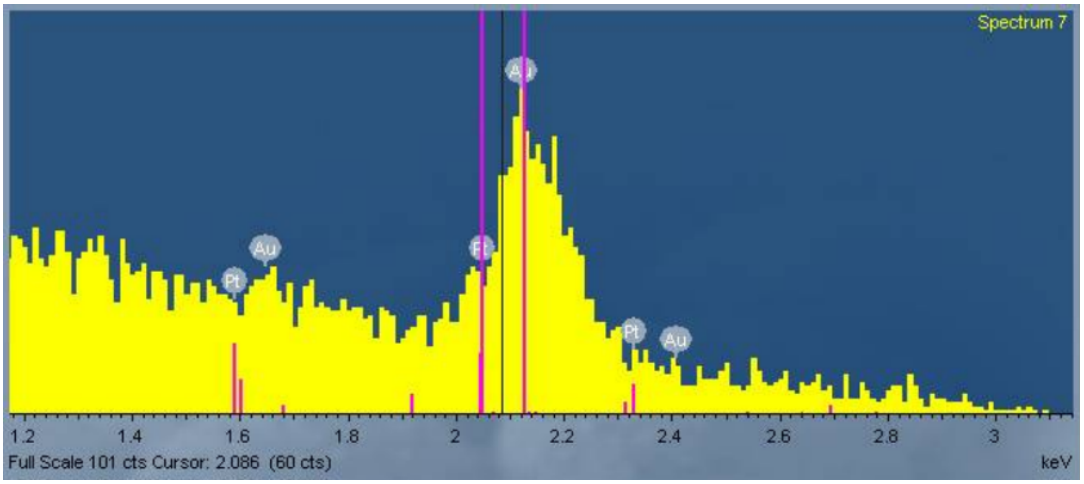

Figure 4.1: SEM–EDX spectrum of Au–Pt nanoparticles. Clear signals are observed in the 2.0–2.3 keV region, corresponding to the overlapping Pt M (≈2.05 keV) and Au M (≈2.12–2.20 keV) lines, confirming the presence of both metals in the sample.

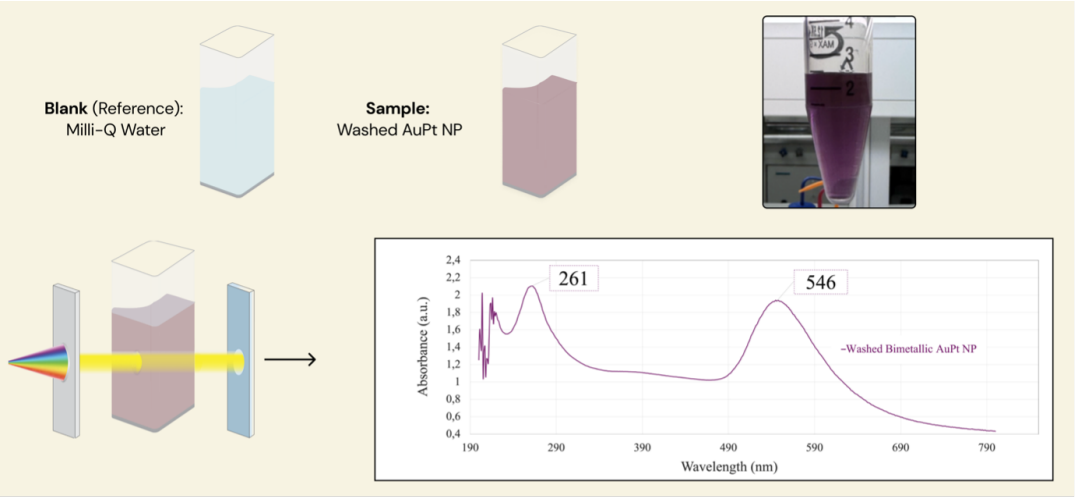

Figure 4.2: UV–Vis characterization of washed bimetallic AuPt nanoparticles. Milli-Q water served as the blank. The transmission spectrum (190–800 nm) shows an absorption feature near 261 nm and a broad LSPR band centered at 546 nm, characteristic of AuPt colloids. The schematic depicts the measurement in transmission, and the photograph shows the purple nanoparticle dispersion after washing. The LSPR signal provides the reference for subsequent immobilization and gas-adsorption studies [48].

4.1.2 UV–Vis Measurements of Au–Pt Nanoparticles

The aim of this experiment is to determine whether AuPt nanoparticles adsorb onto the functionalised surface. As a first step, the UV–Vis spectrum of the AuPt nanoparticle suspension was recorded to identify its characteristic plasmon peaks. Milli-Q (MQ) water was used as the blank because it is the solvent of the suspension. As shown in Figure 4.2, the UV–Vis transmission spectrum exhibits an absorption feature at ∼261 nm and a broad LSPR band centered at ∼546 nm, characteristic of AuPt colloids [46]. The accompanying photograph shows the purple nanoparticle dispersion after washing. This LSPR signal serves as the reference for subsequent immobilization and gas-adsorption studies.

Figure 4.3 compares three UV–Vis spectra: (a) bare quartz, (b) quartz after exposure to the AuPt nanoparticle (NP) suspension, and (c) the AuPt colloid in solution. The bare quartz (blank: air) shows only the silica edge at ∼219 nm and no peak in the visible region. When the coated slide is measured (blank: rinsed quartz), two features appear: a small band at ∼262 nm and a broad plasmon peak at ∼546 nm. These match the peaks of the AuPt colloid (blank: Milli-Q water), showing that the new signals come from immobilized AuPt NPs, not from the substrate or silane. The low absorbance (about 10^{-2} AU) indicates a thin, low-loading film; a slight baseline slope likely reflects weak scattering from the coating. Together, these results confirm successful immobilization and provide the reference spectrum for later gas-adsorption tests.

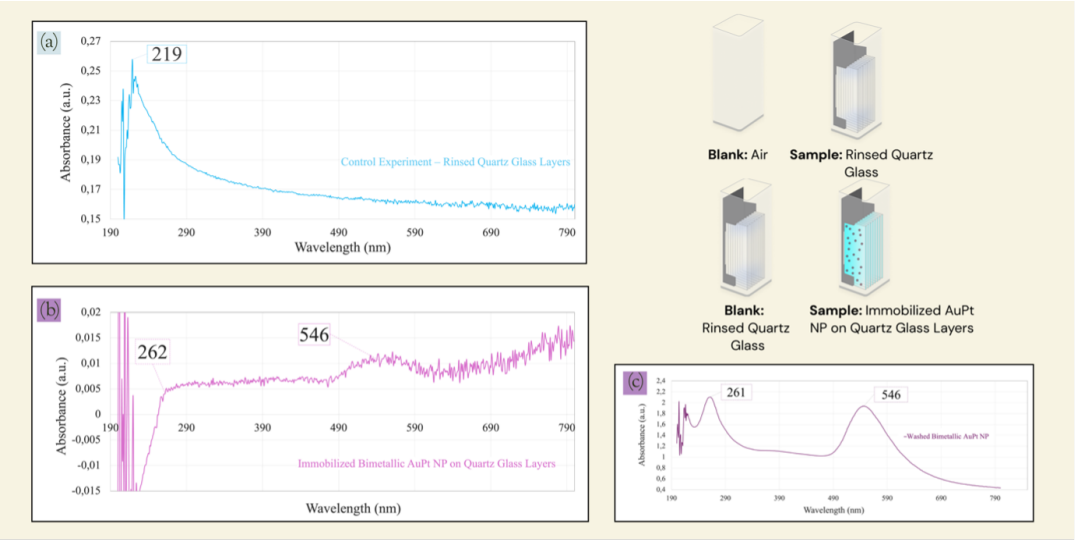

Figure 4.3: UV–Vis verification of AuPt nanoparticle immobilization on quartz. (a) Transmission spectrum of rinsed quartz slides (blank: air) showing no visible-region features and only the silica UV edge near ∼219 nm. (b) Quartz after silanization and exposure to the washed AuPt nanoparticle suspension (blank: rinsed quartz): the emergence of a weak UV band at ∼262 nm and a broad LSPR band centered at ∼546 nm indicates nanoparticle attachment. (c) Reference spectrum of the washed AuPt colloid in solution (blank: Milli-Q water) with bands at ∼261 and ∼546 nm, matching the immobilized film. Schematics on the right illustrate the blanks used for each measurement.

After confirming Au–Pt immobilization on the quartz slides, acetone vapor was introduced to the coated substrates to assess adsorption. As a reference, a UV–Vis spectrum of acetone vapor was first recorded to identify its absorption maximum. The vapor was then introduced to the AuPt-coated quartz slides, the holder was placed in a clean cuvette, and spectra were collected and compared for LSPR peak shifts or intensity changes indicative of adsorption. Figure 4.4 presents the acetone vapor spectrum, the post-exposure spectrum of the AuPt-coated substrate, and the sample/blank configurations used for each measurement.

To see how the coating responds to acetone, we compared the UV–Vis spectra of the immobilized Au–Pt film before and after exposure, focusing on the plasmon region (≈500–620 nm). As highlighted in Figure 4.5, the peak position moves from 536 ± 2 nm to 553 ± 2 nm, a red-shift of ∼17 nm. The peak also becomes broader (FWHM increases from ∼73 nm to ∼112 nm). This red-shift and broadening are consistent with acetone molecules adsorbing on the nanoparticles, which raises the local refractive index around the Au–Pt surface. Measurements used rinsed quartz as the reference; smoothed curves are shown only to help locate the peak.

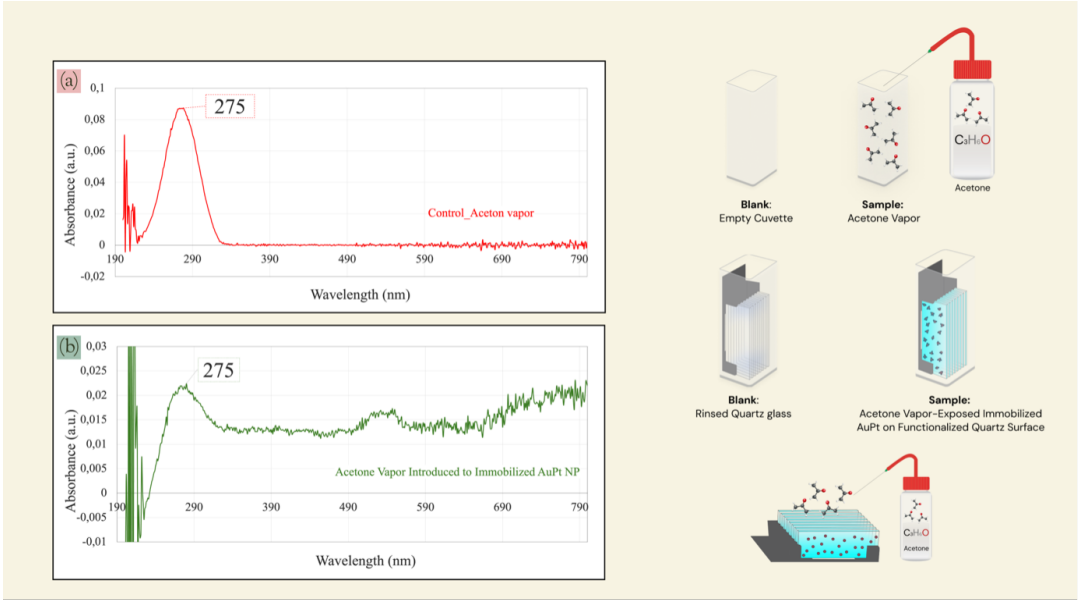

Figure 4.4: UV–Vis response to acetone vapor. (a) Control spectrum of acetone vapor in an empty cuvette (blank: air) showing a strong absorption near 275 nm. (b) Spectrum of Au–Pt–coated, silanized quartz after exposure to acetone vapor (blank: rinsed quartz glass). The 275 nm acetone band is observed together with a slight change across the visible region coincident with the Au–Pt LSPR, consistent with a small adsorption-induced optical response. Schematics on the right illustrate the blank/sample configurations used.

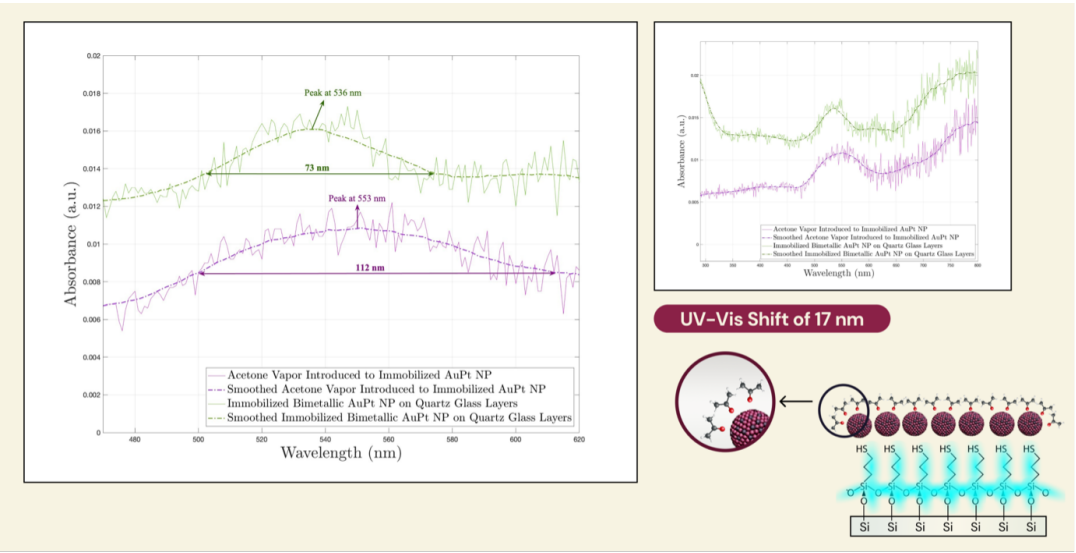

Figure 4.5: UV–Vis of immobilized Au–Pt nanoparticles before and after acetone exposure. The main plasmon peak moves from 536 nm to 553 nm (a 17 nm red-shift) and becomes broader (FWHM 73 → 112 nm). These changes are consistent with acetone molecules adsorbing on the nanoparticle surface and slightly changing the optical environment. (Silanized quartz substrate; rinsed quartz used as the blank.)

To confirm the acetone effect, the entire sample preparation and UV–Vis measurement were repeated three independent times. Spectra were collected in the instrument's high-precision mode (narrow slit, longer integration) to improve signal-to-noise and resolve small changes in the plasmon region (≈480–650 nm). In all runs, the LSPR peak of the immobilized Au–Pt film shifted from ∼529–530 nm (before exposure) to ∼541 nm (after acetone), a red-shift of ∼12 nm, and the peak width changed from ∼115 nm to ∼100 nm (FWHM). Blowing air/N_2 over the acetone-exposed film moved the peak toward its original position, indicating partially reversible adsorption. Smoothed traces are shown only to guide the eye. Figure 4.6 shows the UV–Vis spectra collected in high-precision mode.

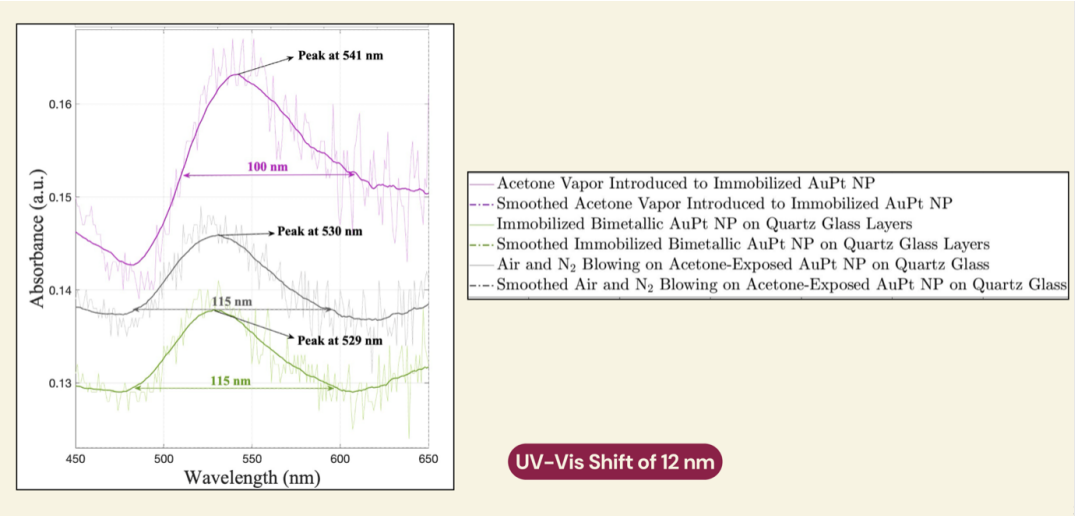

Figure 4.6: Reproducible and partially reversible LSPR response of immobilized Au–Pt to acetone vapor. UV–Vis spectra (high-precision mode) show the LSPR maximum shifting from 529–530 nm (before exposure) to 541 nm after acetone ($\Delta\lambda \approx 12$ nm), with FWHM changing from ∼115 nm to ∼100 nm. Air/N_2 purging moves the peak back toward its original position, indicating partially reversible adsorption. Data shown for three independent repeats; smoothed curves are included to guide the eye.

To ensure that the acetone response originates from the Au–Pt nanoparticles and not from the silane primer, a control experiment was performed on silanized quartz slides without nanoparticles. UV–Vis spectra were recorded for (i) silanized quartz, (ii) the same slides after exposure to acetone vapor, and (iii) after air/N_2 purging, using rinsed quartz as the blank. The three spectra overlap within the noise over 300–800 nm and show no band in the LSPR region (∼500–650 nm), nor any systematic change after acetone exposure or purging; only the quartz UV edge is visible below ∼230 nm. These results indicate that the silane layer does not produce a detectable optical response to acetone, confirming that the shifts observed in earlier figures are due to acetone interacting with the immobilized Au–Pt nanoparticles.

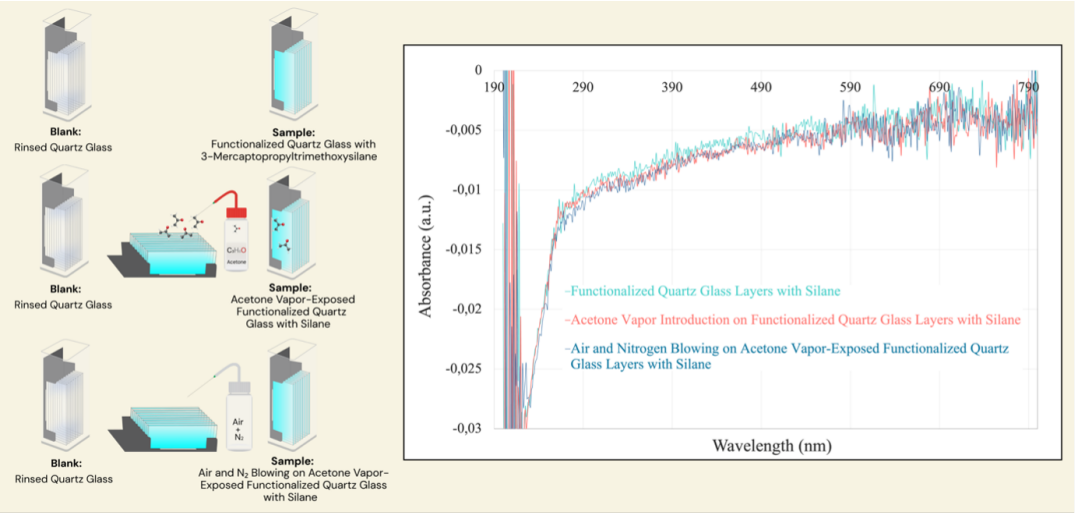

Figure 4.7: Control UV–Vis on silanized quartz (no nanoparticles). Spectra of (i) silanized quartz, (ii) after acetone-vapor exposure, and (iii) after air/N_2 purging (blank: rinsed quartz) overlap across 300–800 nm and show no feature in the 500–650 nm LSPR region. Only the quartz UV edge (<230 nm) is observed, indicating the silane layer does not contribute to the acetone response.

4.1.3 Conclusions for System 1 (Au–Pt Nanoparticles)

Bimetallic Au–Pt nanoparticles were successfully synthesized with uniform, well-dispersed morphology and confirmed composition (SEM/EDX), and then immobilized on silane-functionalized quartz to form optically transparent coatings. UV–Vis spectra of the coated slides reproduced the colloidal plasmon signature, verifying surface attachment. Upon exposure to acetone vapor, the films exhibited a reproducible red-shift and broadening of the LSPR band ($\Delta\lambda \approx 12$–17 nm), consistent with adsorption at the nanoparticle surface and the associated local refractive-index change; partial reversibility was observed upon air/N_2 purging. Together, these results demonstrate (i) controlled synthesis of Au–Pt NPs with uniform shape, (ii) robust immobilization on functionalized substrates, and (iii) measurable acetone interaction, establishing the material's potential as a sensing layer for breath-relevant VOC detection.

4.2 Coordination Cage

To verify immobilization of the cobalt coordination cage on glass, samples were prepared as described in Section 3.2.2 and analysed by UV–Vis spectroscopy. As a baseline control, eight rinsed glass slides were mounted in a rinsed holder, immersed in Milli-Q (MQ) water, and their transmission spectrum was recorded. A matched cuvette containing only MQ water served as the instrumental blank. This control established the optical background of the eight-slide assembly before measuring slides bearing the immobilized cage.

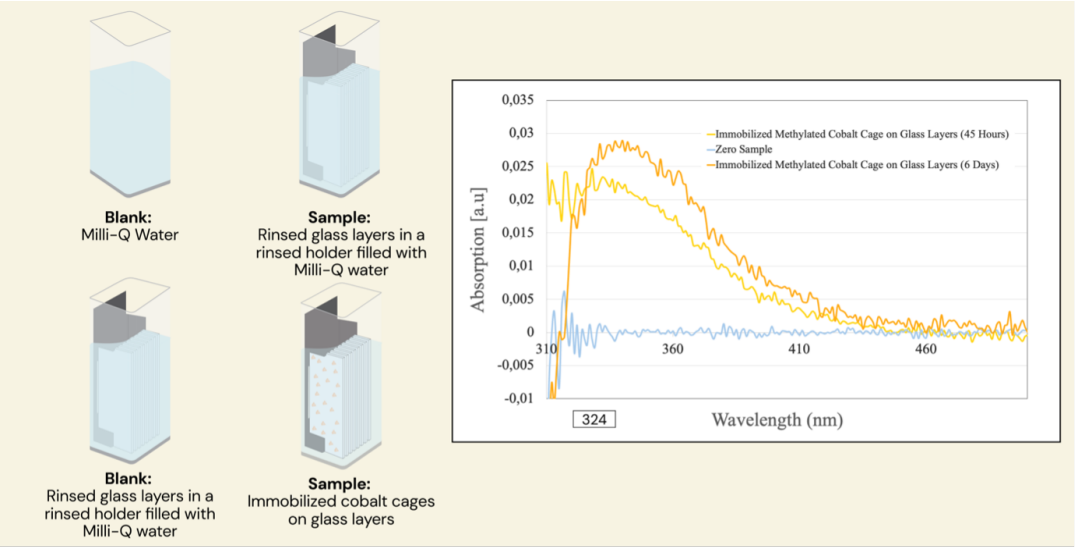

Figure 4.8: UV–Vis verification of methylated Co(II) cage immobilization on glass. Right: transmission spectra using matched blanks (MQ water; rinsed glass in MQ). The coated slides show a characteristic band at ∼324 nm after 45 h (yellow), which persists after 6 days (orange) with a modest decrease in intensity; the zero sample (blue) is featureless. Left: schematics of the blank/sample configurations used.

The baseline spectrum of eight rinsed glass slides immersed in Milli-Q (MQ) water (blank: MQ water) showed no significant absorbance. Slides bearing the immobilized cobalt coordination cage (prepared as in Section 3.2.2) were then mounted in the rinsed holder and immersed in MQ water. For these measurements, a reference blank of eight rinsed glass slides in MQ water was used to remove the substrate contribution. As shown in Figure 4.8, the immobilized-cage assembly exhibits a distinct band at ∼324 nm, matching the solution spectrum of the cobalt cage in Figure 3.13 and confirming successful immobilization on the glass surface.

Given that the sensor will be fabricated on silicon, the following results assess whether the cages immobilize on silicon to a similar extent as on glass.

4.2.1 Immobilization of the Methylated Cobalt(II) Cage on Silicon Substrates

Silicon substrates were cleaned using basic piranha ($NH_4OH/H_2O_2/H_2O$), rinsed with Milli-Q water, dried under N_2, and then immersed in a solution of the methylated Co(II) cage for 24 h at room temperature. This protocol mirrors the glass procedure and was intended to achieve comparable surface coverage on Si. TOF-SIMS subsequently evaluated immobilization.

TOF-SIMS on the coated silicon substrate gives a clear Co^+ signal at $m/z \approx 59$, confirming that cobalt-containing cage molecules are present on the surface. As shown in Fig.25, the optical image reveals some dark spots caused by leftover glue from wafer packaging; although these areas introduce minor local variation, they do not affect the conclusion that the cage is immobilized on silicon.

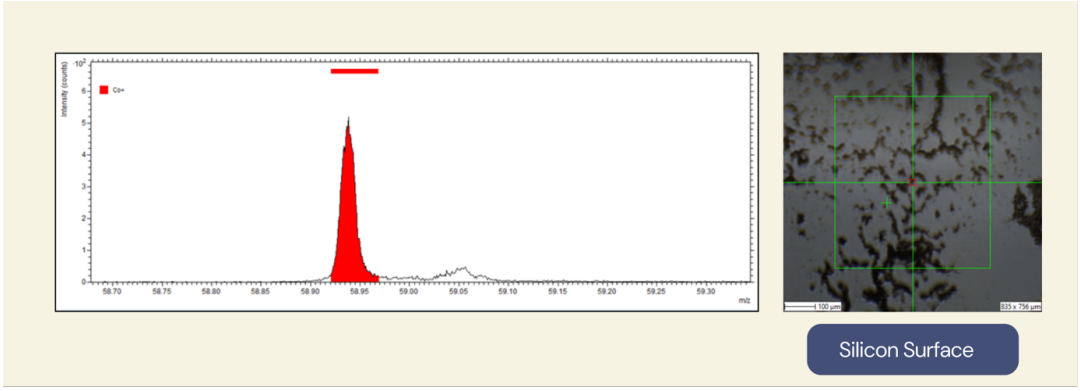

Figure 4.9: TOF-SIMS confirmation of methylated Co(II) cage on silicon. Left: Positive-ion spectrum shows a sharp Co^+ peak at m/z $\approx$ 59, well above background. Right: Optical micrograph of the Si substrate with the analysed ROI (green box); dark patches are residual packaging adhesive not fully removed by the basic piranha clean.

TOF-SIMS measurements were acquired at multiple locations on the silicon sample. As shown in Figure 4.9, a clear Co^+ signal is detected in all regions, confirming that cobalt is present on the wafer. The Co^+ maps are fairly homogeneous over 20 × 20 µm fields of view on the Si areas, indicating uniform coverage. The reported TC (total counts) values provide a semi-quantitative estimate of the total cobalt signal in each map.

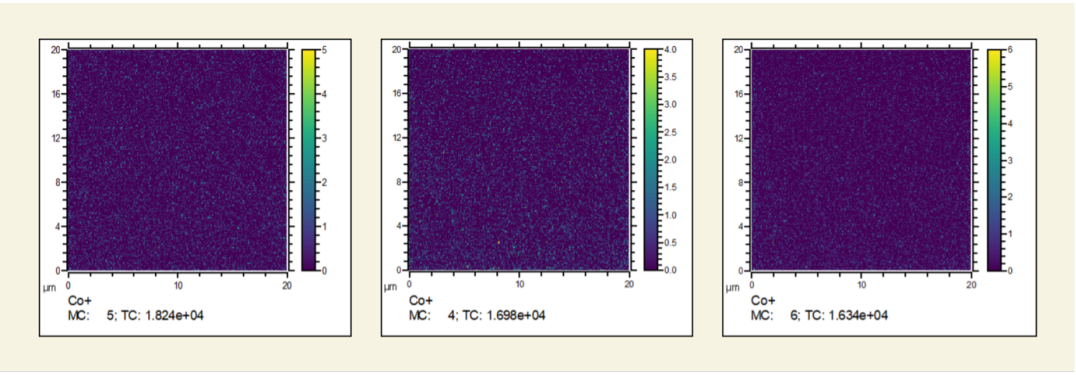

Figure 4.10: TOF-SIMS Co^+ (m/z 59) ion maps for three 20 × 20 μm regions on the silicon wafer after cage immobilization. The maps show a clear, fairly homogeneous cobalt signal across Si areas. TC denotes total Co^+ counts per map, providing a semi-quantitative estimate of surface coverage.

4.2.2 Gas-Molecule Hosting by the Methylated Fe(II) Cage

A D_2O solution of the methylated Fe(II) cage was placed in a septum-sealed glass vial with a stir bar. Gases (N_2, CO_2, H_2, O_2, Ar) were collected in balloons and delivered to the stirred solution through a syringe fitted with a long needle; the needle tip was positioned below the liquid surface to provide gentle, continuous bubbling. Dosing was maintained overnight at room temperature. Immediately afterward, the NMR

tube was filled directly from the gas-equilibrated vial, the tube was sealed, and the sample was taken to the NMR facility and measured by ^{1}H NMR without delay to minimize degassing. This balloon–syringe setup provides steady, near-ambient gas delivery without a dedicated gas manifold.

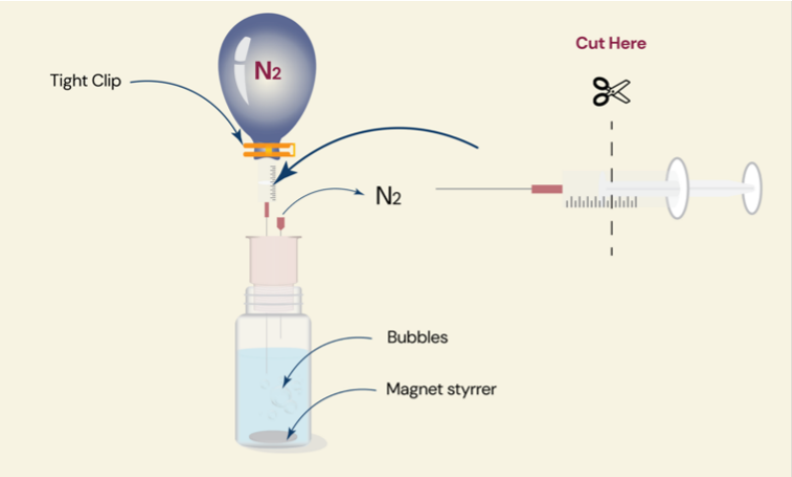

Figure 4.11: Balloon–syringe gas-dosing setup for NMR experiments. Nitrogen (or other gas) is stored in a clipped balloon, passed through a syringe barrel (plunger removed as indicated) and a long needle through the vial septum, and bubbled below the surface of the stirred cage solution. Continuous sparging ensures steady, near-ambient gas delivery.

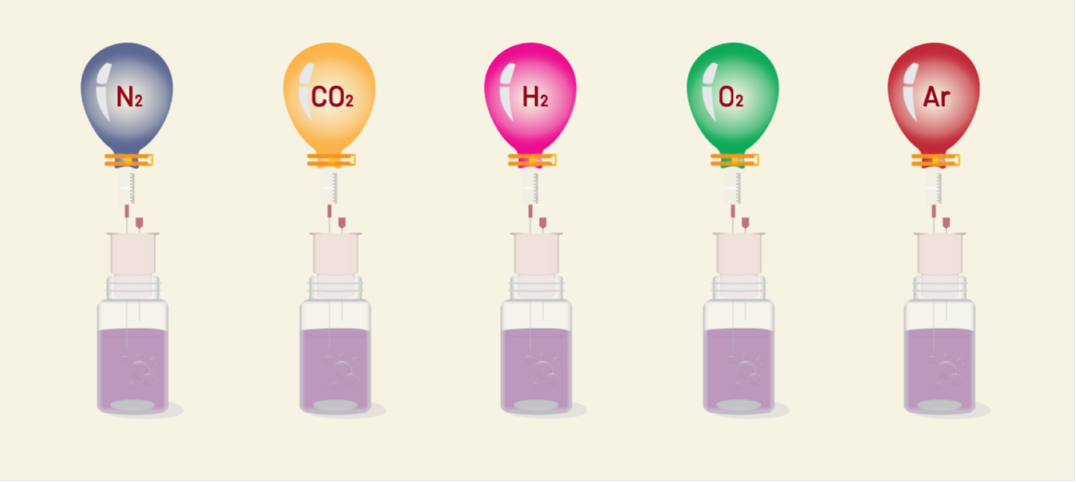

Figure 4.12: Balloon–syringe dosing of gases (N_2, CO_2, H_2, O_2, Ar) into the methylated Fe(II) cage solution for NMR host–guest screening. Each gas was held in a clamped balloon and bubbled through the stirred solution via a syringe needle positioned below the liquid surface before immediate NMR analysis.

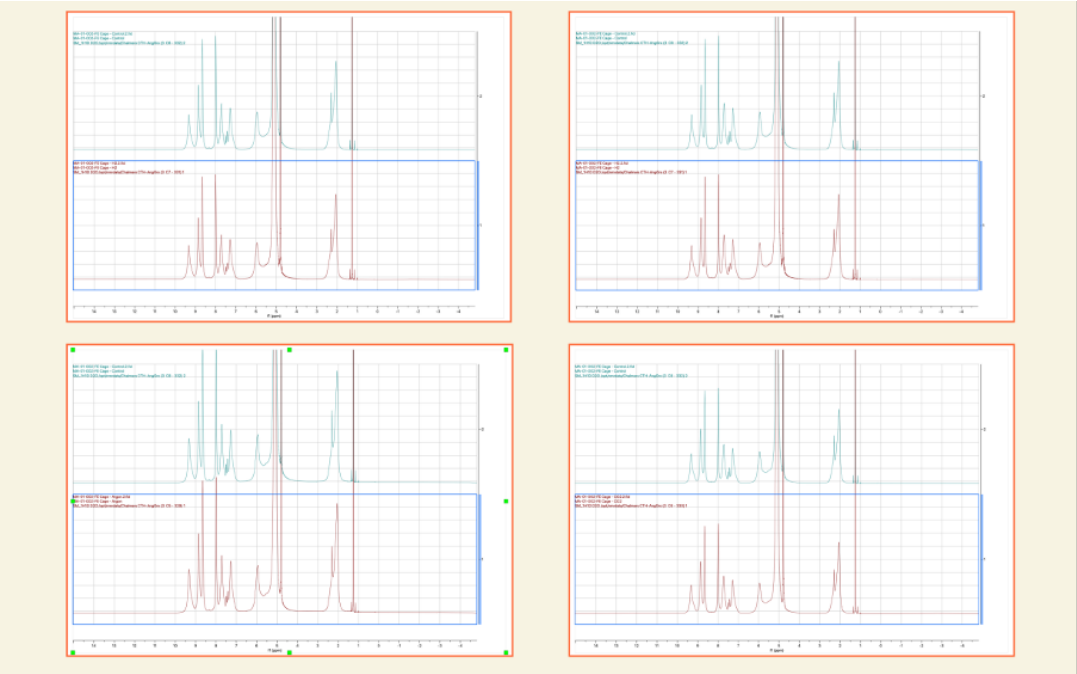

Figure 4.13: Overlaid ^{1}H NMR spectra (D_2O, 298 K) of the methylated Fe(II) cage before (top trace) and after overnight exposure to representative gases (bottom trace; examples shown in the four panels). Across all gases, no resolvable chemical-shift changes, new resonances, or systematic broadening are observed, indicating no detectable host–guest complexation under these ambient conditions.

4.2.3 Proton NMR spectra of gas-exposed methylated Fe(II) cage

Figure 4.13 shows the ^{1}H NMR spectra of the cage solution after exposure to N_2, CO_2, H_2, O_2, and Ar. The spectra look the same as the untreated control, with no clear chemical-shift changes or new peaks are observed. The most likely reason is practical: there was a long delay between gas dosing and NMR measurement, so most dissolved gas probably escaped before the spectra were recorded. It is also possible that any interaction at room temperature and ambient pressure is too weak or too fast to detect by routine ^{1}H NMR.

5
Conclusion

This thesis investigated two material systems, bimetallic gold platinum nanoparticles and a methylated cobalt coordination cage, with the aim of enhancing gas adsorption for future gas sensing applications.

For System 1, AuPt nanoparticles were successfully synthesized using a modified co-reduction method. The resulting nanoparticles showed uniform shape and good dispersion, achieved through careful optimization of synthesis and washing steps. The nanoparticles were effectively immobilized on functionalized quartz substrates, as confirmed by UV-Vis spectroscopy and EDX analysis. Furthermore, UV-Vis measurements after exposure to acetone vapor revealed a measurable shift in the absorbance peak, indicating adsorption of acetone molecules on the immobilized AuPt nanoparticles. These findings demonstrate the potential of AuPt nanostructures as promising materials for sensitive and selective gas sensing.

For System 2, methylated cobalt coordination cages were synthesized and successfully immobilized on both glass and silicon substrates, as verified by UV-Vis and TOF-SIMS analyses. The results confirm successful attachment of the cages to solid surfaces, representing the first demonstration of this specific cage being immobilized on glass and silicon. Although gas hosting studies using NMR did not show a clear signal shift indicating guest encapsulation, the immobilization outcome provides an important step toward integrating such supramolecular systems into solid state gas sensing platforms.

Overall, this work provides insights into two different material approaches for gas adsorption studies, combining nanoscale metallic systems with molecular cage structures. These findings form a foundation for future development of advanced gas sensors that unite high sensitivity with molecular selectivity.

Bibliography

[1] Marfatia, K., Ni, J., Preda, V. and Nasiri, N., 2025. Is Breath Best? A Systematic Review on the Accuracy and Utility of Nanotechnology Based Breath Analysis of Ketones in Type 1 Diabetes. Biosensors, 15(1), p.62.

[2] Wei, J., Liu, T., Huang, J., Li, X., Qi, Y. and Luo, G., 2024. Detection of Acetone as a Gas Biomarker for Diabetes Based on Gas Sensor Technology. arXiv preprint arXiv:2406.00993.

[3] Bulemo, P.M., Kim, D.H., Shin, H., Cho, H.J., Koo, W.T., Choi, S.J., Park, C., Ahn, J., Guntner, A.T., Penner, R.M. and Kim, I.D., 2025. Selectivity in Chemiresistive Gas Sensors: Strategies and Challenges. Chemical reviews, 125(8), pp.4111-4183.

[4] Ochoa-Muñoz, Y.H., Mejía de Gutiérrez, R. and Rodríguez-Páez, J.E., 2023. Metal oxide gas sensors to study acetone detection considering their potential in the diagnosis of diabetes: a review. Molecules, 28(3), p.1150.

[5] Mortazavi, S., Makouei, S., Abbasian, K. and Danishvar, S., 2025, August. Exhaled Breath Analysis (EBA): A Comprehensive Review of Non-Invasive Diagnostic Techniques for Disease Detection. In Photonics (Vol. 12, No. 9, p. 848). MDPI.

[6] Wang, H., Duan, P., Tian, J., Duan, Q., Jin, K. and Sun, J., 2025. Synergistic effect of bimetallic Au-Pt functionalized In2O3 nanoflowers for ppb-level hydrogen detection. Sensors and Actuators B: Chemical, 426, p.137082.

[7] Britto Hurtado, R., Cortez-Valadez, M., Flores-Lopez, N.S. and Flores-Acosta, M., 2020. Agglomerates of Au-Pt bimetallic nanoparticles: synthesis and antibacterial activity. Gold Bulletin, 53(2), pp.93-100.

[8] Omidvar, A. and Soleymani, H., 2025. Designing Bimetallic Sensors for Acetone Biomarker Detection. ACS omega, 10(13), pp.12953-12960.

[9] Zhu, X., Cao, P., Li, P., Yu, Y., Guo, R., Li, Y. and Yang, H., 2024. Bimetallic PtAu-Decorated SnO2 Nanospheres Exhibiting Enhanced Gas Sensitivity for Ppb-Level Acetone Detection. Nanomaterials, 14(13), p.1097.

[10] La Cognata, S. and Amendola, V., 2023. Recent applications of organic cages in sensing and separation processes in solution. Chemical Communications, 59(92), pp.13668-13678.

[11] Skugor Roncevic, I., Vladislavic, N., Chatterjee, N., Sokol, V., Oliver, C.L. and Kukovec, B.M., 2021. Structural and electrochemical studies of cobalt (II) and nickel (II) coordination polymers with 6-oxonicotinate and 4, 4-bipyridine. Chemosensors, 9(12), p.352.

[12] Ward, M.D., Hunter, C.A. and Williams, N.H., 2018. Coordination cages based on bis (pyrazolylpyridine) ligands: structures, dynamic behavior, guest binding, and catalysis. Accounts of Chemical Research, 51(9), pp.2073-2082.

[13] Chen, R., Yao, Z., Han, N., Ma, X., Li, L., Liu, S., Sun, H. and Wang, S., 2020. Insights into the adsorption of VOCs on a cobalt-adeninate metal–organic framework (Bio-MOF-11). ACS omega, 5(25), pp.15402-15408.

[14] Huang, Y., Zhang, T., Xu, T., Peng, Z., Xu, Y. and He, S., 2024. Monitoring Acetone with Photoacoustic Spectroscopy Using a Metal–Organic Framework. Advanced Optical Materials, 12(10), p.2302280.

[15] Liu, C., Zhang, Y. and An, Q., 2021. Functional material systems based on soft cages. Chemistry–An Asian Journal, 16(10), pp.1198-1215.

[16] Wang, Z.Q., Luo, H.Q., Wang, Y.L., Xu, M.Y., He, C.T. and Liu, Q.Y., 2021. Octanuclear Cobalt (II) Cluster-Based Metal–Organic Framework with Caged Structure Exhibiting the Selective Adsorption of Ethane over Ethylene. Inorganic Chemistry, 60(14), pp.10596-10602.

[17] Matic, E.S., Bernard, M., Jernstedt, A.J. and Grommet, A.B., 2024. Orthogonal Phase Transfer of Oppositely Charged FeII4L6 Cages. Chemistry–A European Journal, 30(71), p.e202403411.

[18] Dubost, E., Dognon, J.P., Rousseau, B., Milanole, G., Dugave, C., Boulard, Y., Léonce, E., Boutin, C. and Berthault, P., 2014. Understanding a Host–Guest Model System through 129Xe NMR Spectroscopic Experiments and Theoretical Studies. Angewandte Chemie International Edition, 53(37), pp.9837-9840.

[19] Zhao, H., Li, J., She, X., Chen, Y., Wang, M., Wang, Y., Du, A., Tang, C., Zou, C. and Zhou, Y., 2024. Oxygen vacancy-rich bimetallic Au@ Pt core–shell nanosphere-functionalized electrospun ZnFe2O4 nanofibers for chemiresistive breath acetone detection. ACS sensors, 9(4), pp.2183-2193.

[20] Shin, K.Y., Kim, Y., Mirzaei, A., Kim, H.W. and Kim, S.S., 2025. Bimetal-decorated resistive gas sensors: a review (Mar, 10.1039/D5TC00145E, 2025). JOURNAL OF MATERIALS CHEMISTRY C, 13(20), pp.10434-10436.

[21] Martins, C.S., Sousa, H.B. and Prior, J.A., 2021. From impure to purified silver nanoparticles: Advances and timeline in separation methods. Nanomaterials, 11(12), p.3407.

[22] Wu, H., Zeng, R., Li, L., Li, M., Zhu, Y., Li, W., Zhao, B., Wen, C. and Feng, F., 2025. Exhaled Gas Biomarkers: A Non-Invasive Approach to Distinguishing Diabetes and Its Complications. Analyst.

[23] Dlamini, N.G., Basson, A.K. and Pullabhotla, V.S.R., 2023. Synthesis and characterization of various bimetallic nanoparticles and their application. Applied Nano, 4(1), pp.1-24.

[24] Esparza, R., Rosas, G., Valenzuela, E., Gamboa, S., Pal, U. and Pérez, R., 2008. Structural analysis and shape-dependent catalytic activity of Au, Pt and Au/Pt nanoparticles. Matéria (Rio de Janeiro), 13, pp.579-586.

[25] Nuti, S., Fernández-Lodeiro, J., Palomo, J.M., Capelo-Martinez, J.L., Lodeiro, C. and Fernández-Lodeiro, A., 2024. Synthesis, Structural Analysis, and Peroxidase-Mimicking Activity of AuPt Branched Nanoparticles. Nanomaterials, 14(13), p.1166.

[26] Lehn, J.M., 1988. Supramolecular chemistry—scope and perspectives molecules, supermolecules, and molecular devices (Nobel Lecture). Angewandte Chemie International Edition in English, 27(1), pp.89-112.

[27] Ariga, K. and Kunitake, T., 2006. Supramolecular chemistry—fundamentals and applications: Advanced textbook. Berlin, Heidelberg: Springer Berlin Heidelberg.

[28] Kolesnichenko, I.V. and Anslyn, E.V., 2017. Practical applications of supramolecular chemistry. Chemical Society Reviews, 46(9), pp.2385-2390

[29] R. W. Saalfrank, A. Stark, K. Peters, and H. G. von Schnering, "The First 'Adamantoid' Alkaline Earth Metal Chelate Complex: Synthesis, Structure, and Reactivity," Angewandte Chemie International Edition in English, vol. 27, no. 6, pp. 851–853, Jun. 1988, doi: https://doi.org/10.1002/anie.198808511.

[30] McConnell, A.J., 2022. Metallosupramolecular cages: from design principles and characterisation techniques to applications. Chemical Society Reviews, 51(8), pp.2957-2971.

[31] Percástegui, E.G., Ronson, T.K. and Nitschke, J.R., 2020. Design and applications of water-soluble coordination cages. Chemical Reviews, 120(24), pp.13480-13544.

[32] Zhang, D., Ronson, T.K., Zou, Y.Q. and Nitschke, J.R., 2021. Metal–organic cages for molecular separations. Nature Reviews Chemistry, 5(3), pp.168-182.

[33] Y. Fang et al., "Catalytic reactions within the cavity of coordination cages," Chem Soc Rev, vol. 48, no. 17, pp. 4707–4730, Aug. 2019, doi: 10.1039/C9CS00091G.

[34] Cullen, W., Misuraca, M.C., Hunter, C.A., Williams, N.H. and Ward, M.D., 2016. Highly efficient catalysis of the Kemp elimination in the cavity of a cubic coordination cage. Nature Chemistry, 8(3), pp.231-236.

[35] Mal, P., Breiner, B., Rissanen, K. and Nitschke, J.R., 2009. White phosphorus is air-stable within a self-assembled tetrahedral capsule. Science, 324(5935), pp.1697-1699.

[36] W. Meng et al., "A Self-Assembled M8L6 Cubic Cage that Selectively Encapsulates Large Aromatic Guests," Angewandte Chemie International Edition, vol. 50, no. 15, pp. 3479–3483, Apr. 2011, doi: 10.1002/ANIE.201100193.

[37] Zarra, S., Clegg, J.K. and Nitschke, J.R., 2013. Selective assembly and disassembly of a water-soluble Fe10L15 prism. Angewandte Chemie, 125(18), pp.4937-4940.

[38] T. K. Ronson, S. Zarra, S. P. Black, and J. R. Nitschke, "Metal–organic container molecules through subcomponent self-assembly," Chemical Communications, vol. 49, no. 25, pp. 2476–2490, Feb. 2013, doi: 10.1039/C2CC36363A.

[39] P. Mal et al., "An Unlockable–Relockable Iron Cage by Subcomponent Self-Assembly," Angewandte Chemie International Edition, vol. 47, no. 43, pp. 8297–8301, Oct. 2008, doi: 10.1002/ANIE.200803066.

[40] Wang, K.Y., Zhang, J., Hsu, Y.C., Lin, H., Han, Z., Pang, J., Yang, Z., Liang, R.R., Shi, W. and Zhou, H.C., 2023. Bioinspired framework catalysts: From enzyme immobilization to biomimetic catalysis. Chemical Reviews, 123(9), pp.5347-5420.

[41] Lorzing, G.R., Gosselin, A.J., Trump, B.A., York, A.H., Sturluson, A., Rowland, C.A., Yap, G.P., Brown, C.M., Simon, C.M. and Bloch, E.D., 2019. Understanding gas storage in cuboctahedral porous coordination cages. Journal of the American Chemical Society, 141(30), pp.12128-12138.

[42] Percástegui, E.G., 2022. Metal–organic cages against toxic chemicals and pollutants. Chemical Communications, 58(33), pp.5055-5071.

[43] Keeler, J., 2010. Understanding NMR spectroscopy. John Wiley ,and Sons.

[44] Ward, M.D., 2024. New insights into coordination-cage based catalysis. Chemical Communications.

[45] Benninghoven, A., 1994. Chemical analysis of inorganic and organic surfaces and thin films by static time-of-flight secondary ion mass spectrometry (TOF-SIMS). Angewandte Chemie International Edition in English, 33(10), pp.1023-1043.

[46] Jawad, M., Ali, S., Waseem, A., Rabbani, F., Amin, B.A.Z., Bilal, M. and Shaikh, A.J., 2019. Plasmonic effects and size relation of gold-platinum alloy nanoparticles. Advances in nano research, 7(3), p.169.

[47] Akash, M.S.H. and Rehman, K., 2019. Ultraviolet-visible (UV-VIS) spectroscopy. In Essentials of pharmaceutical analysis (pp. 29-56). Singapore: Springer Nature Singapore.

[48] Butt, M.A., 2025. Surface plasmon resonance-based biodetection systems: principles, progress and applications—a comprehensive review. Biosensors, 15(1), p.35.

DEPARTMENT OF CHEMISTRY AND CHEMICAL ENGINEERING
Division of Applied Chemistry
CHALMERS UNIVERSITY OF TECHNOLOGY
Gothenburg, Sweden
www.chalmers.se

CHALMERS
UNIVERSITY OF TECHNOLOGY